International Journal of Heat and Mass Transfer 183 (2022) 122019

Contents lists available at ScienceDirect

International Journal of Heat and Mass Transfer

journal homepage: www.elsevier.com/locate/hmt

Analytic characterization and operational limits of a hybrid two-phase mechanically pumped fluid loop based on the capillary pumped loop

Julio Ferreira[a], Benjamin Furst[b], Takuro Daimaru[b], Eric Sunada[b], Massoud Kaviany[a,*]

[a] Department of Mechanical Engineering, University of Michigan, Ann Arbor, MI 48109
[b] Jet Propulsion Laboratory/California Institute of Technology, Pasadena, California, 91101

ARTICLE INFO

Article history:
Received 1 March 2021
Revised 9 September 2021
Accepted 26 September 2021

Keywords:
Pumped loop heat pipe
Dryout limit
Flooding limit
Phase distribution
Stability
Transient

ABSTRACT

Two-phase mechanically pumped fluid loops have the potential to provide numerous benefits for spacecraft based applications. Here a hybrid two-phase capillary and mechanically pumped fluid loop that shows promise for spacecraft thermal control applications is analyzed and its operational limits are characterized. Data from an experimental system that incorporates a 3D printed evaporator is correlated to several models that together provide a comprehensive characterization of the system behavior. The loop performance is analyzed using pointwise as well volume-averaged governing equations and resistance network models, to predict flooding and dryout limits. Also, system-level numerical (including 3-D CFD simulations) transient and linear-response analyses are performed predicting the changing loop phase distributions and the observed time-dependent behavior. With the 3D-printed evaporator, a notably high evaporator conductance of 30 W/cm^2-K and heat flux over 10 W/cm^2 over large area are achieved with negligible temperature non-uniformity.

1. Introduction and background

The increasingly ambitious human and robotic exploration of our solar system requires the development of advanced thermal control technologies in order to sustain extra-terrestrial vehicles in extreme environments [1]. Two-phase thermal control systems such as heat pipes and loop heat pipes (LHP) are considered some of the most effective thermal control systems currently available and are commonly used on spacecraft due to their high thermal conductance per unit mass [2]. Over the past several decades, there has been an effort to extend the capability of two-phase thermal control systems through the development of two-phase mechanically pumped fluid loops for spacecraft [3]. NASA has formally identified the development of a two-phase mechanically pumped fluid loop as an enabling technology for certain missions [1]. In pursuit of this goal, NASA JPL is currently developing a two-phase mechanically pumped fluid loop for spacecraft systems to enable the next generation of solar system exploration [1].

Many two-phase mechanically pumped fluid loop architectures have been proposed for spacecraft systems each with different strengths and weaknesses [4]. The two-phase MPFL discussed here is a derivative of the system first proposed by Park et al. in 2005 [5] and with minor variations by Hoang et al. in 2007 [6]. This class of two-phase MPFLs are hybrid systems that utilizes both a mechanical pump as well as capillary pumping in the evaporator. In particular, they include the addition of a mechanical pump and bypass line to enhance the system operating characteristics. These systems have their heritage in the Capillary Pumped Loop (CPL) largely developed by NASA in the 1980's [7] and the subsequent hybrid capillary-mechanically pumped heat transport systems developed in the following years [3]. CPLs and the closely related Loop Heat Pipe (LHP) are limited in their operation due to their reliance on the capillary pumping provided in the evaporator-pump. The addition of the bypass line and mechanical pump supplement the pumping capability of the evaporator pump and allow for transporting larger quantities of heat over longer distances as well as enable the accommodation of higher heat fluxes [8,9]. Several investigations have explored the hybrid CPL discussed here with encouraging results [5,6,3]. The particular embodiment of the system discussed here was first presented in 2019 [8]. Positive attributes of this system include minimal power requirements, minimal two-phase flow regions, and operational robustness [8]. These are critical attributes for spaceborne systems where power, predictability and robustness are crucial.

This class of hybrid mechanical/capillary pumped loops contrasts with the majority of two-phase MPFLs developed for engi-

* Corresponding author.
E-mail address: kaviany@umich.edu (M. Kaviany).

https://doi.org/10.1016/j.ijheatmasstransfer.2021.122019
0017-9310/

Nomenclature

A	area (m^2)
C_2	inertial resistance coefficient (1/m)
c_p	specific heat (J/kg-K)
D	diameter (m)
f	friction factor
g	gravity (m/s^2)
h	height (m)
Δh_{lg}	heat of evaporation (J/kg)
$\boldsymbol{J}$	Jacobian matrix
K	permeability (m^2)
k	thermal conductivity (W/m-K)
L, l	length (m)
M	mass (kg)
$\dot{M}$	mass flow rate (kg/s)
$\dot{m}$	mass flux (kg/m^2-s)
N, n	number of plates, number of divisions
Nu	Nusselt number
p	pressure (Pa)
Pe	Péclet number
Pr	Prandtl number
Q	heat load (W)
q	heat flux (W/m^2)
R_t	thermal resistance (K/W)
R_u	hydraulic resistance [Pa/(kg/s)]
Re	Reynolds number
S_i	source term ($kg/m^{2-}s^2$)
r	radius (m)
T	temperature (°C)
t	time (s)
u	velocity (m/s)
V	volume (m^3)
W, w	width (m)
x	vapor quality
$\boldsymbol{x}$	state vector
$\boldsymbol{x_o}$	equilibrium point
Greek Symbols	
α	thermal diffusivity (m^2/s)
δ	liquid thickness (m)
Δ	variation
ε	porosity
ϵ	surface roughness
η	eigenvector
κ	eigenvector of the transposed Jacobian
λ	eigenvalue (1/s)
μ	viscosity (Pa-s)
ρ	density (m^3/kg)
σ	surface tension (N/m)
τ	time constant (s)
θc	contact angle (º)
Subscripts	
a	accumulator
amb	ambient
b	boil-off
c	capillary, condenser
CHF	critical heat flux
$c-v$	capillary-viscous
d	dryout
e	evaporator
f	coolant, flooding
g	gas/vapor
h	heater
i	inlet
l	liquid
lg	saturation
m	mass
max	maximum
n	nominal
o	outlet
p	pore, plate
ph	preheat
s	surface, solid
sh	superheat
t	thermal
u	hydraulic
w	wick
Others	
$\langle\ \rangle$	spatial average

neering applications that utilize a “mixed-flow” design where the working fluid is exclusively circulated by a mechanical pump and partially vaporized in the evaporator. These “mixed-flow” designs lead to the presence of two-phase flow in the transport line between the evaporator and the condenser [10]. The presence of two-phase flow in the transport line has three negative implications for space born systems: (1) two-phase flow is notoriously hard to predict in microgravity; (2) two-phase flow has larger pressure drop and consequently requires more pumping power; and (3) two-phase flow is prone to multiple instabilities [11,12]. The hybrid two-phase MPFL architecture described here largely avoids these issues by avoiding the development of two-phase flow in the transport lines.

The hybrid mechanically pumped fluid loop (MPFL) considered here is shown in Fig. 1(a) with its main components, control devices and sensors. The pump is upstream of the 3D-printed evaporator (phase-change line) and the liquid bypass lines. Fig. 1(b) shows the schematic loop diagram with the key thermal and hydraulic resistances. The key loop variables are marked in red.

Starting at the pump exit, loop point 1, the system branches into two main lines: the phase-change and bypass lines. In the phase-change line are located the 3D-printed evaporator and the condenser, which are connected by the vapor line. The flow rate in this line (under stable operation) is pure vapor and determined by the heat load on the evaporator (as in a CPL), with any extra flow directed through the bypass line (a needle valve determines the pressure drop). Loop points 2 and 3 are the evaporator inlet and outlet. The two lines merge downstream from the condenser, at point 4, and an additional heat exchanger is used to provide subcooling. An accumulator is located between the subcooler exit, point 5, and the pump inlet, point 6.

The thermodynamic state in the accumulator is externally controlled, thus setting the pressure reference for the system (fixing the saturation condition in the evaporator). Further details are provided in [8,13].

Here, a numerical model of the system is developed and the operational limits are examined. In particular, the flooding, dryout, liquid boil off and wick superheat limits are defined for the system. Additionally, operational stability regimes of the system are characterized using steady-state and transient analyses (including linear response). The results of the analysis are shown to agree with experimental data acquired during a test campaign of a breadboard system developed at NASA JPL .

We begin with a description of the key components in the breadboard two-phase mechanically pumped fluid loop as well as the tests used to explore the operational limits of the system. The

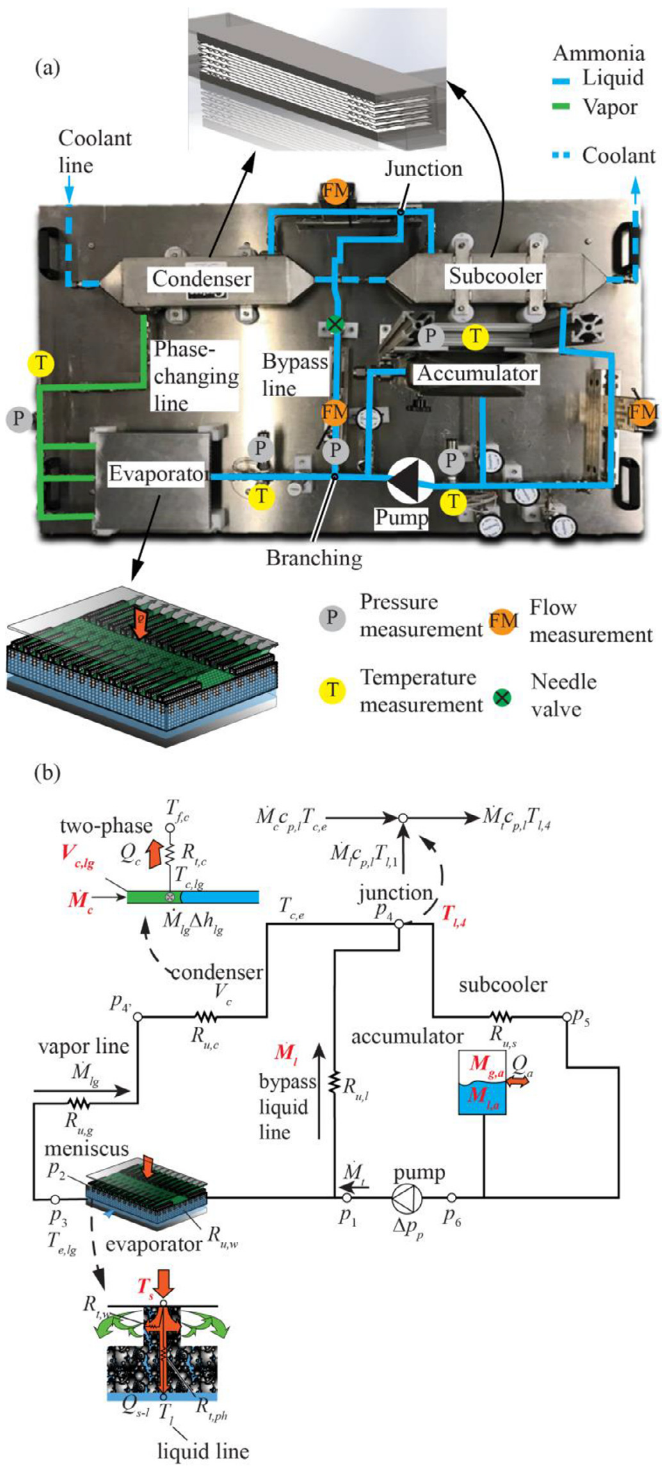

Fig. 1. (a) Physical image, and (b) schematic of the JPL MPFL showing the key loop components, controls, and sensors. The schematic also highlights the key loop variables (e.g., mass flow rates, pressures and temperatures) and hydraulic and thermal resistances. The red marked variables are use in the dynamical analysis.

remainder of the paper focuses on the analysis and which define the operational limits of the system. Finally, it is shown that the predicted steady-state and transient behavior allow for estimation of the 3D-printed evaporator permeability and maximum capillary pressure, which are in agreement with their estimates by other means (e.g., CFD simulations).

2. JPL two-phase MPFL and data

2.1. Loop components

A. *Evaporator*

A unique monolithic planar 3D printed evaporator is used in the system, that is operationally similar to a CPL evaporator [13]. The evaporator is a critical component in the loop, and estimation of its effective thermal conductivity $\langle k\rangle$ and permeability are discussed in Appendix A. The wick thermal resistance is

$$R_{t,w} = \frac{\langle\delta\rangle_w}{\langle k\rangle A_{lg}}, \tag{1}$$

where $\langle\delta\rangle_w$ is the average distance from the heater to the evaporating meniscus, given in Table 1, validated with bask surface IR imaging from [8] and $A_{lg} = w_g l_g$ is the cross-sectional area of vapor path, symmetry conditions were used, thus using half distances, illustrated in Fig. 2.

The evaporator is made from a 3D-printed aluminum alloy using is compatible with ammonia (the breadboard working fluid). The additive manufacturing method Direct Metal Laser Sintering (DMLS) is used, allowing suitable selection of alloys and proven ability to produce porous wicking structures [14]. Two similar evaporator designs with the same composition were used and are schematically shown in Fig. 2 alongside a SEM micrograph of the wick structure. The SEM was taken from an unused sample manufactured from the same batch as evaporator 2, using the same parameters and materials for DMLS, so it is representative of the evaporator 2 wick. Thin layers of fine metal powder (particle size in the order 60 µm) are deposited on a build plate and a laser is used to fuse the metal powder in that layer in the controlled regions, building the part by layers. The process occurs layer-by-layer, from the bottom to the top. The DMLS allows for part density to be varied from fully dense to porosities up to 40%, making it suitable for manufacturing a complex two-phase loop evaporator such as those shown in Fig. 2 [15].

Both evaporators have a set of vapor channels that are separated from the liquid channels with a porous wick, however Evaporator 1 has wick material between the heated surface and the vapor channels, while Evaporator 2 has an array of porous fins that meet the heated surface. The pore-size related data will be discussed in Appendix A (Section A.2). The second design with the porous fins bounding the vapor channel, evaporator 2, supports higher operation pressures (up to 1.39 MPa). The manufactured evaporator 2 is illustrated in Fig. 3(a). Fig. 3(b) shows a CAD view of this 3D-printed evaporator and a schematic representation of the porous fins that bound the vapor channel.

The capillary pressure of the 3D-printed wick, aided by the forced liquid flow pressure drop across the bypass line, balances the pressure drop in the vapor line and the wick (evaporator), i.e.,

$$p_c = \; p_3 - p_2 = \dot{M}_{lg}(R_{u,g} + R_{u,w}) - \dot{M}_l R_{u,l}, \tag{2}$$

where the pressure drop across the vapor line, wick, and bypass line are the product of the mass flow rate and the hydraulic resistance, $\Delta p_i = \dot{M}_i R_{u,i}$. The sum of the vapor line and wick hydraulic resistances is the phase-change line resistance, and the hydraulic resistance of the bypass line is determined by the needle valve, which provides an additional control to accommodate the pressure drop that surpasses the maximum capillary pressure at high heat loads The gravity effect (hydrostatic pressure) is negligible, since all loop components were arranged horizontally. The hydrostatic pressure within the wick is $< 0.1 p_{c,max}$ and within the accumulator is $< 0.05 p_{c,max}$. The pressure differential between the accumulator and the system is due to temperature difference (26 °C and 20 °C).

Table 1
JPL LHP parameters and conditions, including hydraulic and thermal resistances, and mass and geometric parameters of the components.

Hydraulic resistances		Thermal resistances and cooling loop parameters		Accumulator		Condenser				Evaporator			
$R_{u,l}$, Pa/(kg/s)[1]	1.8×10^{5}	$R_{t,e}$, °C/W	3.16×10^{-4}	$M_{a,0}$, kg	0.06	$A_{c,c}$, m^2	1.64×10^{-5}	W_p, mm	101.6	L_e, mm	200	h_g, mm	1
$R_{u,w}$, Pa/(kg/s)	1.9×10^{6}	$R_{t,c}$, °C/W	3.39×10^{-3}	V_a, m^3	0.0065	A_p, m^2	0.307	L_p, mm	299.0	W_e, mm	200	w_g, mm	1
$R_{u,g}$, Pa/(kg/s)	3.3×10^{6}	$R_{t,s}$, °C/W	3.39×10^{-3}			M_c, kg	6.28	h_c, mm	1.6	h_l, mm	1	M_e, kg	1
$R_{u,c}$, Pa/(kg/s)	3.3×10^{6}	$T_{f,c}$, K	293.15			V_c, m^3	2.4×10^{-4}	$N_{c,1}/N_{c,2}$	5/5	h_w, mm	4	$\langle\delta_w\rangle$, mm	0.67

[1] Bellows-sealed metering valves Technical Manual [19].

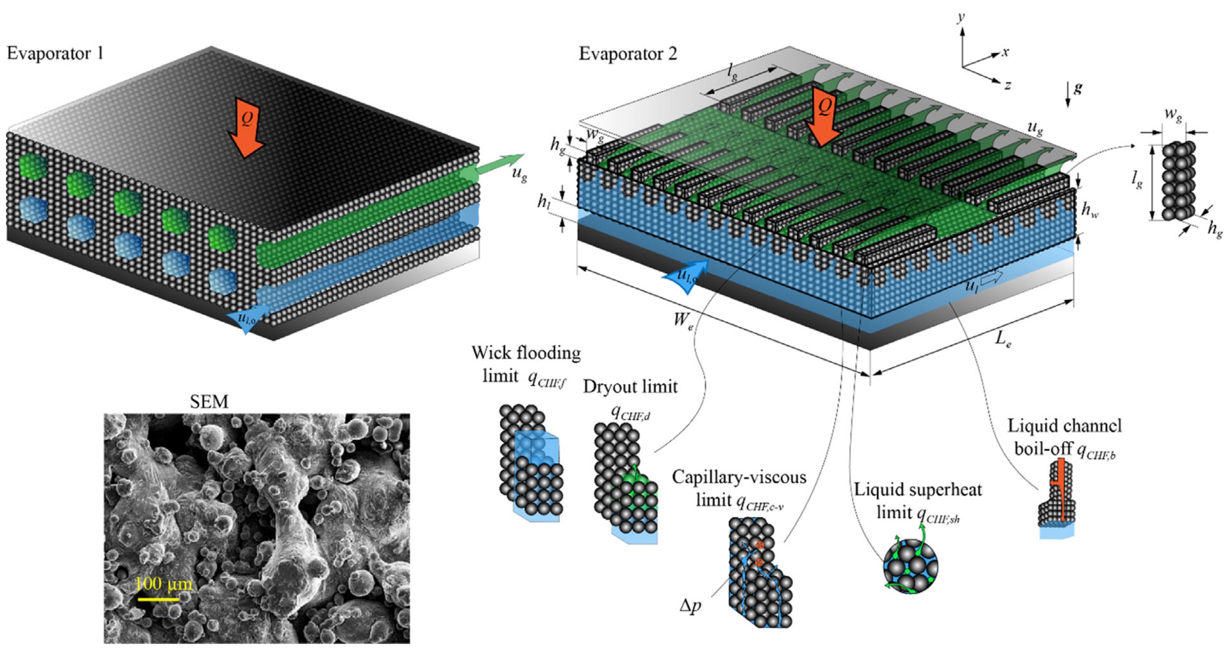

Fig. 2. Schematic of a section of the evaporators 1 and 2 and their geometric parameters. The SEM micrograph of the evaporator wick surface is also shown. At the bottom, the evaporator wick relevant operational limits ae shown.

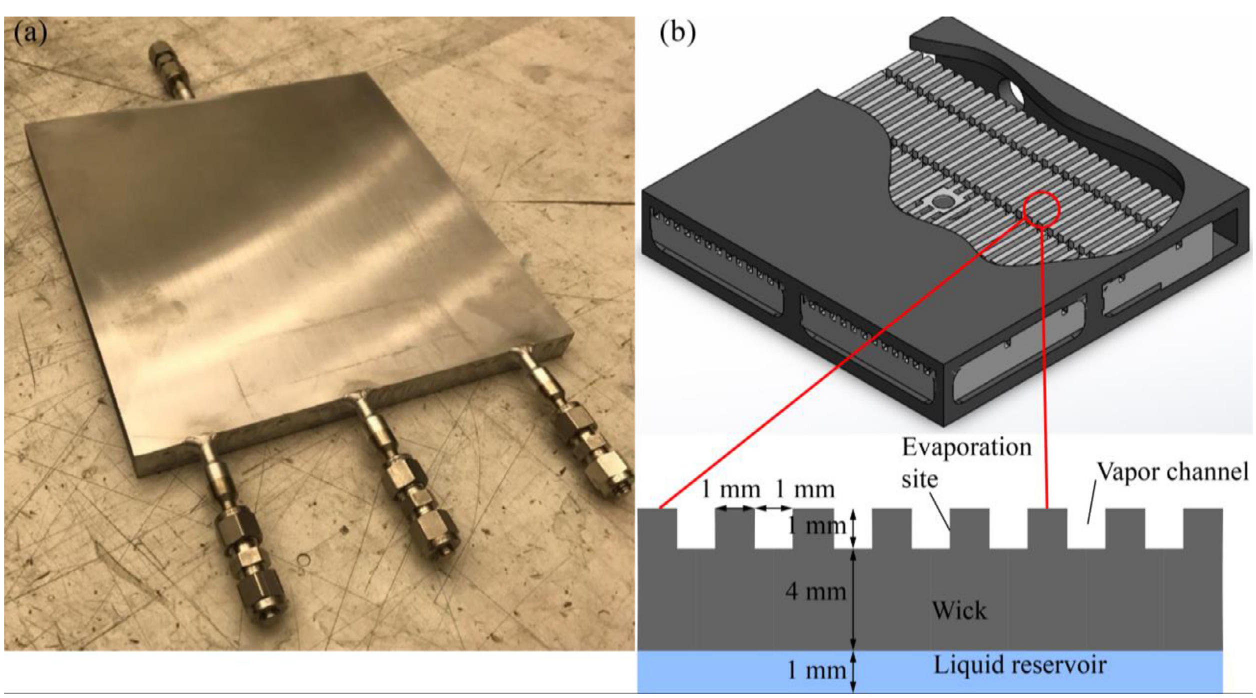

Fig. 3. (a) 3D-printed evaporator assembled with casing showing the single liquid inlet and three vapor inlets. (b) CAD view of the 3D-printed evaporator with schematic representation detailing the wick geometry, highlighting evaporation sites and vapor channel.

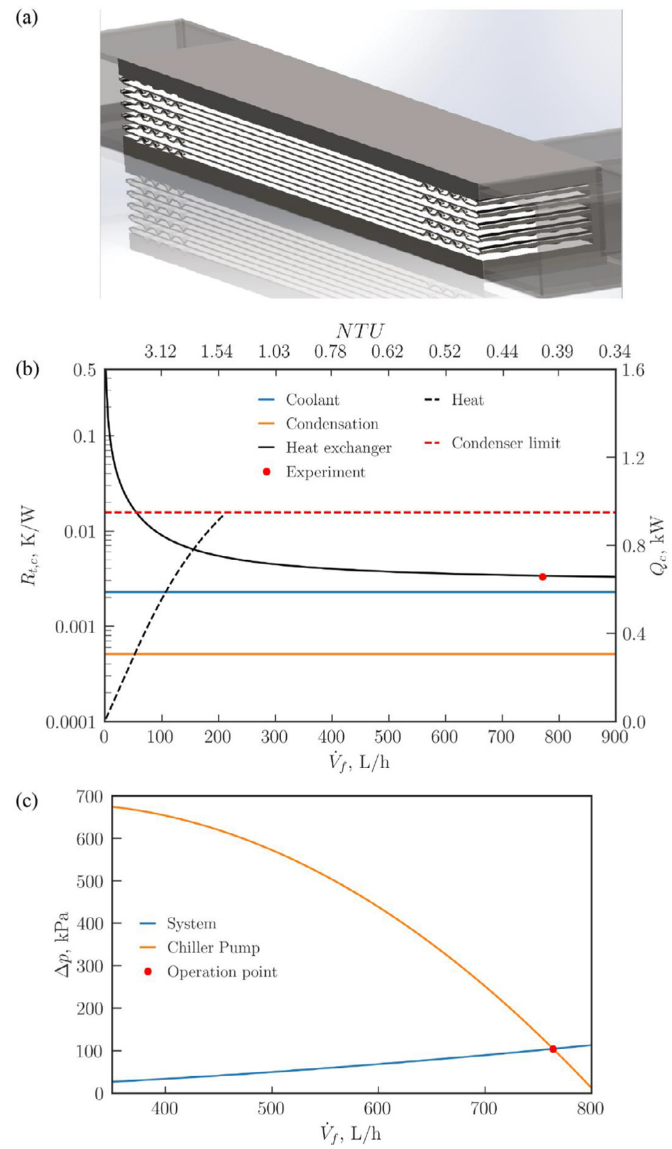

Fig. 4. (a) Physical image of the dimpled plate condenser heat exchanger with a longitudinal cut. Performance variations of condenser (b) overall thermal resistance and heat flow rate, and (c) pressure drop with respect to the coolant volumetric flow rate. An operational point at high coolant flow rate is also marked.

The evaporator is subject to several dryout limits illustrated in Fig. 2, mainly the capillary-viscous (and the superheat/boil-off) limit determined by the wick design, and the dryout/flooding limits which depend on the loop performance.

Capillary-viscous limit, $q_{CHF,c-\nu}$: this is under no mechanical pumping, where the maximum capillary pressure (occurs in the monolayer) is balanced by the summation of all viscous and inertial pressure drops occurring along the liquid and vapor paths (which depend on the mass flux).

Wick flooding and dryout limits, $q_{CHF,f}$ and $q_C HF, d$: these occur under hybrid operation and when the dynamic pressure difference across the wick is large enough to force extra (over the capillary-only flow) liquid across the wick or prevents the wick from pumping the liquid due to excessive vapor flow resistance.

The other limits are discussed in Appendix B.

B. *Condenser*

A cutaway image of the condenser and subcooler dimpled-plate heat exchanger is shown in Fig. 4(a). The heat exchanger thermal resistance is [16]

$$\langle R_{t,he} \rangle = \frac{1}{\left(\dot{M}c_p\right)_{min} \epsilon_{he}}, \tag{3}$$

with the heat exchanger effectiveness calculated as $\epsilon_{he} = 1 - e^{-NTU}$ and the number of transfer units

$$NTU = \frac{1}{R_\Sigma \left(\dot{M}c_p\right)_{min}}, \tag{4}$$

and the overall resistance R_Σ is the series combination of the surface-convection resistance in each stream

$$R_\Sigma = R_{c,1} + R_{c,2}. \tag{5}$$

$$R_{c,i} = \frac{D_h}{A_p k_l \mathrm{Nu}_{D,h}}, \tag{6}$$

with the geometric parameters are listed in Table 1. The Nusselt number for the coolant side takes into account the dimple enhancement [17]

$$\frac{\mathrm{Nu}_{D,h}}{\mathrm{Nu}_o} = 1.2341 \left(\frac{S_L}{S_T}\right)^{0.0827} \left(\frac{S_T}{D}\right)^{0.0206}, \tag{7}$$

where $S_L = 8.7$ mm is the dimple longitudinal spacing, $S_T = 3.8$ mm is the dimple transversal spacing, $D = 7.78$ mm is the dimple diameter, and Nu_o is the Nusselt number for two parallel plates with no dimples, $\mathrm{Nu}_o = 7.54$ for fully-developed laminar flow ($Re_{D,h} < 2300$). The Reynolds number based on the hydraulic diameter and the Prandtl number are

$$Re_{D,h} = \frac{\rho_l u_l D_h}{\mu_l}, \quad \mathrm{Pr} = \frac{\mu_l c_{p,l}}{k_l}, \tag{8}$$

On the working fluid side, the phase-change Nusselt number is [16]

$$\mathrm{Nu}_{D,h} = \begin{cases} 5.03 Re_{l,eq}^{1/2} \mathrm{Pr}_l^{1/3}, & Re_{l,eq} < 5 \times 10^4 \\ 0.0265 Re_{l,eq}^{4/5} \mathrm{Pr}_l^{1/3}, & Re_{l,eq} > 5 \times 10^4 \end{cases}, \tag{9}$$

where the equivalent Reynolds number is

$$Re_{l,eq} = \frac{\dot{m}_{eq} D_h}{\mu_l}, \tag{10}$$

and the equivalent mass flux is

$$\dot{m}_{eq} = \dot{m}_f \left[(1-x) + x \left(\frac{\rho_l}{\rho_g}\right)^{1/2} \right], \tag{11}$$

with $x = \dot{m}_g / \dot{m}_f$ is the vapor (thermodynamic) quality.

The condenser thermal resistance is shown in Fig. 4(b) as a function of the volumetric flow rate. At high coolant flow rates, the heat exchanger resistance reaches a plateau. The red circle in Fig. 4(b) denotes the baseline resistance used to match the results from [13,8]. The coolant volumetric flow rate was determined from the chiller pump and the variations of coolant-line pressure drop with volumetric flow rate are shown in Fig. 4(c), alongside the chiller pump curve from the manufacturer manual [18]. The coolant operation point is about 3.4 gal/min or 770 L/h.

C. *Pump*

The mass flow rate in the system is controlled by the pump speed. From Fig. 5, the operation point is identified as the intersection of the pressure drop in the system with any of the pump curves. The system curve is determined by points 1–4–5–6–1 in Fig. 1(b). The lengths of segments are given in [8] and the pipe diameter $D = 4.57$ mm. The pressure drop is calculated using the Darcy-Weisbach equation [20]

$$\Delta p = f \frac{\rho_l u_l^2}{2} \frac{L}{D}, \tag{12}$$

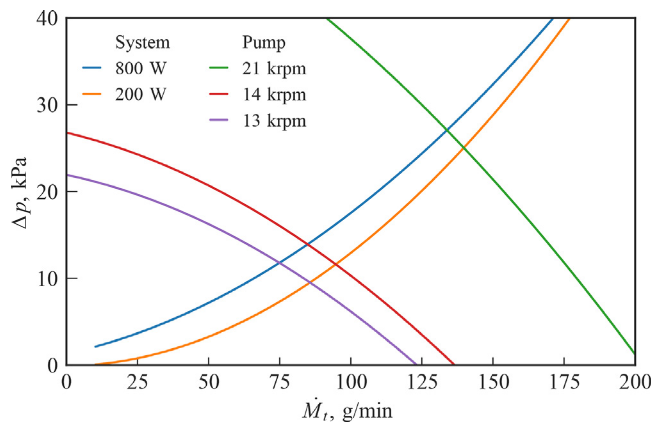

Fig. 5. Performance variations of pump pressure drop with respect to the mass flow rate, for three pump rpm values. The system pressure drop curve for two different heat loads is also shown. Note that the larger heat load has a smaller pressure drop due to the relative configuration of hydraulic resistances in the vapor and bypass lines.

where f is the friction factor, calculated as $f = 64/Re_l$ if $Re_l < 2300$, otherwise the Colebrook-White equation [21,22]

$$\frac{1}{f_l^{1/2}} = -2\log\left(\frac{\epsilon}{3.7D} + \frac{2.51}{Re_l f_l^{1/2}}\right). \tag{13}$$

with

$$Re_l = \frac{\rho_l \langle u_l \rangle L}{\mu_l}. \tag{14}$$

is used. All bends were assumed to be 90°, with an equivalent length of 30D each. The adopted valve resistance in the bypass line is shown in Table 1, determined from the manufacturer [19]. For each flowmeter, the quadratic relation available in [8] is used.

Fig. 5 shows the pump curve for three different rotations and the system curve for two different input heat loads. Since there is a valve with a large pressure drop resistance in the bypass line, by reducing the mass flow rate through it (increasing Q), the system pressure drop is also reduced.

By varying the pump speed, the operation point jumps between performance curves, this can be used to assess the stability of the system. The pump rotation is an additional control parameter.

D. *Accumulator*

The accumulator model is shown in Fig. 6, with the initial state as

$$V_{l,0} = \frac{M_a - \rho_g V_a}{\rho_l - \rho_g}, \tag{15}$$

$$V_{g,0} = V_a - \frac{M_a - \rho_g V_a}{\rho_l - \rho_g}, \tag{16}$$

where M_a is the total mass in the accumulator at $t = 0$ s, and V_a is the accumulator volume. From the time integration of the entire system, the mass leaving the accumulator to compensate for heat input is

$$\Delta M_{l,1} = -\left(\frac{Q_{lg}}{\Delta h_{lg}} - \frac{Q_c}{\Delta h_{lg}}\right)\Delta t, \tag{17}$$

where Q_{lg} and Q_c are the heat absorbed in the evaporation and rejected at the condenser. The thermodynamic state is determined by the external control (fixed accumulator saturation state), so there is no vapor expansion (which requires additional fraction of liquid evaporating to occupy the vapor space). From the volume and mass conservation in the accumulator, we have

$$\Delta V_g = -\Delta V_{l,1} = -\frac{\Delta M_{l,1}}{\rho_l}, \tag{18}$$

$$\Delta M_{g,a} = \rho_g \Delta V_g = -\frac{\rho_g}{\rho_l}\Delta M_{l,1}, \tag{19}$$

$$\Delta M_{l,2} = -\Delta M_{g,a}. \tag{20}$$

Although the phase-change kinetics is not modelled here, it is assumed instantaneous. This is justified since the time constant associated with interfacial evaporation is much smaller than the thermal time constants discussed in Section 5. The total liquid mass change in the accumulator is

$$M_{l,a,f} - M_{l,a,o} = \Delta M_{l,1} + \Delta M_{l,2} = -\left(1 + \frac{\rho_g}{\rho_l}\right)\left(\frac{Q_{lg}}{\Delta h_{lg}} - \frac{Q_c}{\Delta h_{lg}}\right)\Delta t. \tag{21}$$

These relations area also used in transient form to complete the system modeling.

2.2. Operational limits

The evaporator dictates the dominant limits of the hybrid CPL operation, and its design is illustrated in Fig. 2. The wick maximum capillary pressure is based on the maximum surface pore radius [13]

$$p_{c,max} = \frac{2\sigma\cos\theta}{r_{pore}}. \tag{22}$$

The micrograph in Fig. 2 shows large surface pores up to 108 µm, which correspond to a $p_{c,max} = 300$ Pa. This value is also verified by a CFD analysis of pressure drop in the evaporator wick. The contact angle for ammonia-aluminum was taken as the same as that for acetone-aluminum, $\theta = 19.4°$ [13], a conservative approach since most authors use $\theta = 0°$ The surface tension is $\sigma = 20$ mN/m, and varies less than 4% in the range of saturation temperature considered.

The pressure drop in a porous media by the Darcy law is [23]

$$\Delta p = \frac{\mu_l \langle u_l \rangle L}{K_w} = \dot{M}_{lg}\frac{\mu_l L}{\rho_l A K_w}, \tag{23}$$

where the term multiplying the mass flow rate is the wick hydraulic resistance $R_{u,w}$.

The vapor-line pressure drop uses the Colebrook-White expression from Eq. (13) with the so-called unified model [24,25], with a single relation covering the entire range (laminar, transition, and turbulent) of Reynolds number

$$Re_g = \frac{\rho_g \langle u_g \rangle D}{\mu_g}. \tag{24}$$

with switch functions to interpolate between the regimes. In [25] a unified model smoothly captures the transitions between flow regimes, resulting in a more accurate pressure drop and follows the inflectional shape [26], showing a slight decrease in the friction factor before reaching the maximum value governed by the roughness. The tube roughness is estimated to be $\varepsilon = 0.002$ mm.

The capillary-viscous dryout limit is related to $p_{c,max}$, and from Eq. (2)

$$q_{CHF,c-v} = \frac{\Delta h_{lg}\left[p_{c,max} + \left(\dot{M}_{lg} + \dot{M}_l\right)R_{u,l}\right]}{A_h\left(R_{u,g} + R_{u,l} + R_{u,w}\right)}. \tag{25}$$

For $R_{u,l} = 0$, this give the capillary-flow-only heat flux limit.

When the bypass-line pressure drop is too large, such that the evaporator wick can no longer control the flow rate in the phase-change line, the evaporator becomes flooded. The flooding limit is the low heat load operation limit. The capillary pressure is the difference between the vapor and liquid pressures across the meniscus. When the sign of this pressure difference changes, the meniscus inversion is observed.

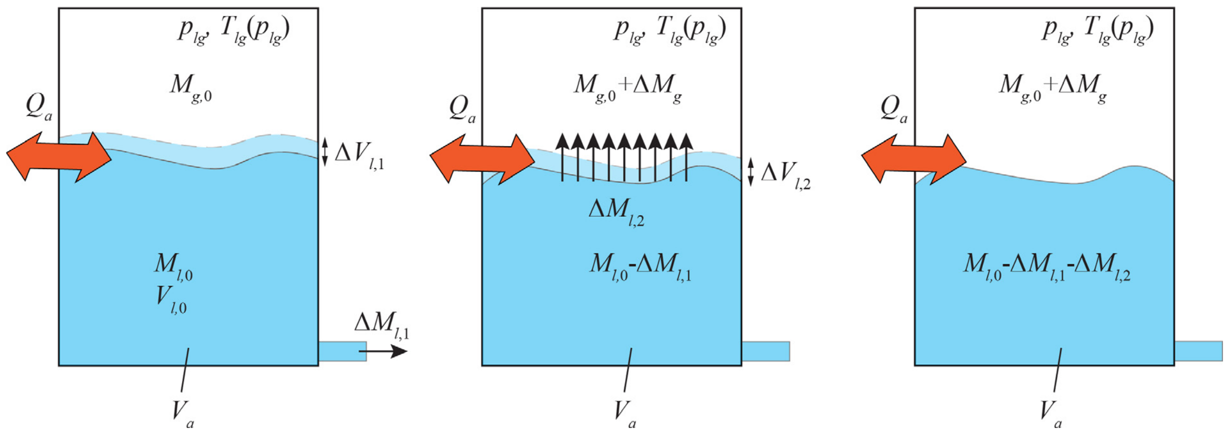

Fig. 6. Schematic of the accumulator model showing the changes in the liquid and vapor volumes in response to heat input/withdrawal. It is assumed the fluid remains in saturated state.

Table 2
Range of liquid flow rate and heat load in evaporator 1 and 2 tests and observed operational limits.

Evaporator	$\dot{M}_t$(g/min)	Q(W)	Operational limit
1	90–210	60–850	Dryout, flooding
2	90	100–400	Dryout, flooding

Dryout occurs when the pressure difference across the meniscus is larger than the maximum capillary pressure, predicted by Eq. (22). Similarly, flooding occurs when this pressure difference becomes negative. In Eq. (2), i.e., the pressure difference across the wick has to be larger than zero, and the flooding limit, i.e., the minimum heat flux, is

$$q_{CHF,f} = \frac{\Delta h_{lg}\left(\dot{M}_{lg} + \dot{M}_l\right)R_{u,l}}{A_h(R_{u,g} + R_{u,l} + R_{u,w})}. \tag{26}$$

From Eq. (26), under no resistance in the bypass line, the flooding limit is zero, i.e., as long as there is heat load, no flooding is observed. This is an idealization, and the flooding limit does depend on the bypass-valve arrangement. Flooding is also affected by the vapor pressure variation inside the evaporator.

The flooding and dryout limits are well established in the experimental data. (The wick superheating $Q_{CHF,sh}$ and liquid channel boil-off $Q_{CHF,b}$ are discussed in Appendix B).

2.3. Loop test data

The time variations in the measured temperature, heat load, and mass flow rate are shown in Fig. 7 for tests with the two evaporator designs. The observed oscillations in the vapor mass flow rate and the evaporator inlet temperature are investigated below. Table 2 summarizes the range of test conditions. Instabilities such as mass flow rate-induced flooding and heat load-induced dryout are observed. Fig. 7(a) shows the time variations in mass flow rate, heat load and temperature measurements for evaporator 1 (Test 23). The oscillations observed in the vapor mass flow rate and in the evaporator inlet temperature for $t > 6$ h correspond to the flooding instability. The same variables are shown in Fig. 7(b) for a test with evaporator 2 (Test 47). The spike in the evaporator outlet temperature for $t < 6$ h corresponds to the dryout limit. Transient prediction of the flooding and dryout events and their mechanisms will be addressed in Sections 4 and 5.

3. Steady state analysis and operating regimes

Following the schematic shown in Fig. 1(b) with the relevant hydraulic and thermal resistances, the conservation and state conditions applied to each component and at the junctions are:

evaporator (e) mass conservation

$$\dot{M}_{lg} = \frac{Q_{lg}}{\Delta h_{lg}}, \tag{27}$$

momentum balance – wick pressure drop

$$p_1 - p_2 = \dot{M}_{lg}R_{u,w}, \tag{28}$$

energy balance

$$Q = Q_{lg} + Q_{ph} = \dot{M}_{lg}\Delta h_{lg} + \dot{M}_{lg}c_{p,l}\left(T_{e,lg} - T_l\right), \tag{29}$$

$$Q_{lg} = \frac{T_s - T_{e,lg}}{R_{t,e}}, \tag{30}$$

thermodynamics – equation of state for saturated ammonia [27].

vapor line (g)

$$p_3 - p_{4'} = \dot{M}_{lg}R_{u,g}, \tag{31}$$

condenser (c) - mass conservation

$$\dot{M}_c = \frac{Q_c}{\Delta h_{lg}}, \tag{32}$$

momentum balance

$$p_{4'} - p_{4''} = \dot{M}_c R_{u,c}, \tag{33}$$

energy balance, $R_{t,c} = f(Q_{lg})$

$$Q_c = \frac{V_{c,lg}}{V_c}\frac{\left(T_{c,lg} - T_{f,c}\right)}{R_{t,c}}, \tag{34}$$

Thermodynamics (ideal gas and Clausius-Clapeyron equations)

$$p = \rho_g R_g T \ , \tag{35}$$

$$\frac{1}{T_{c,lg}} - \frac{1}{T_{lg,3}} = \frac{-R_g}{M_m \Delta h_{lg}} \ln\left(\frac{p_{4'}}{p_3}\right), \tag{36}$$

adiabatic liquid mixing junction (j) - mass conservation

$$\dot{M}_t = \dot{M}_{lg} + \dot{M}_l, \tag{37}$$

momentum balance

$$p_1 - p_4 = \dot{M}_l R_{u,l}, \tag{38}$$

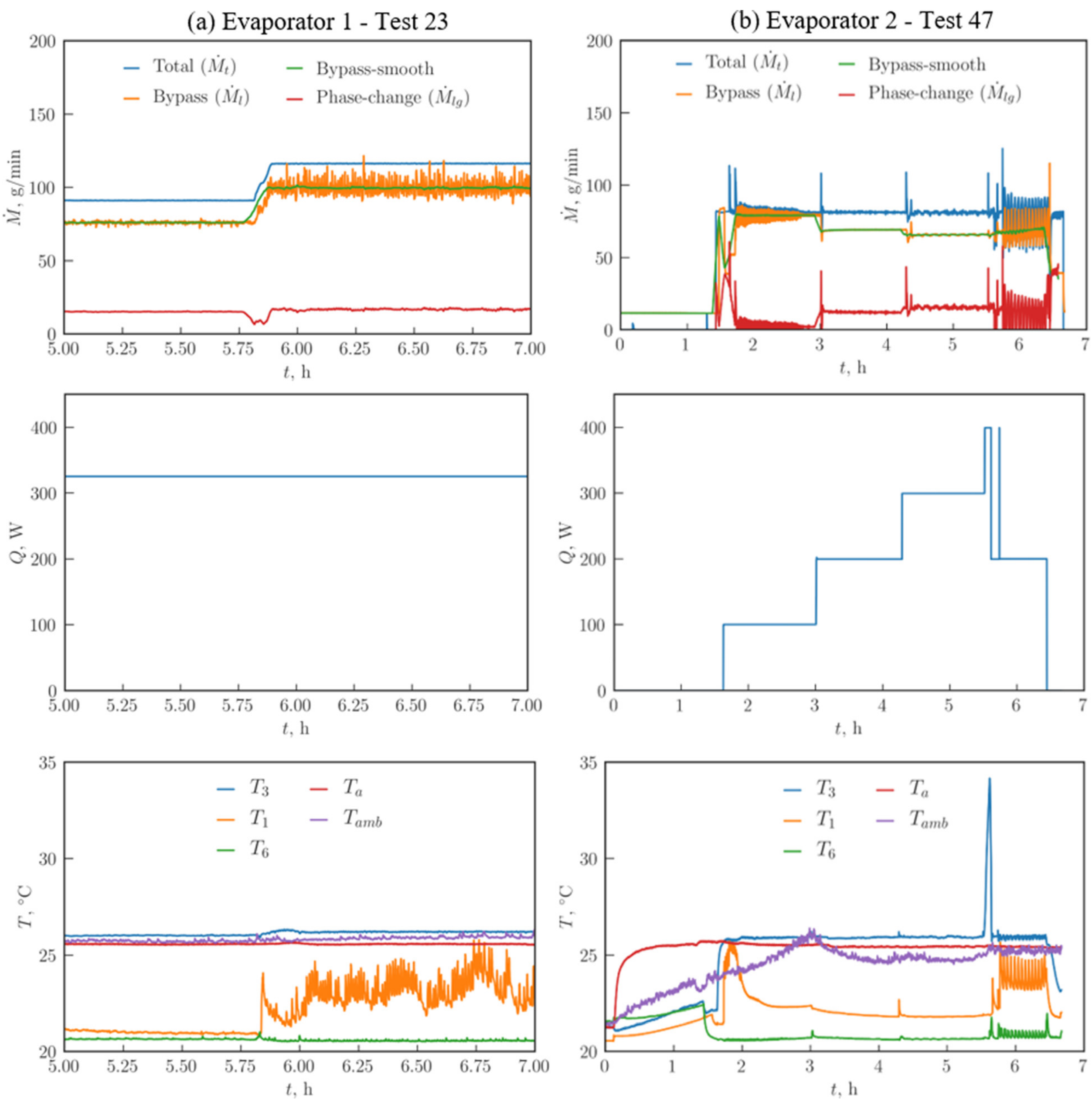

Fig. 7. Measured time variations of the mass flow rates, heat load, and temperatures for Tests (a) 23, and (b) 47. The mass flows include the total, liquid bypass line (with smoothened presentation), and vapor line. The temperatures designation corresponds to Fig. 1(b). These excerpts of test data illustrate nominal steady state behavior for different heat loads (Test 47, 1.6 hr to 5.6 hr), dryout (Test 47, 5.7 hr), flooding due to a change in mass flowrate (Test 23, 5.8 hr) and residual oscillations from a dryout event (Test 47, > 6 hr).

energy balance

$$\dot{M}_t c_{p,l} T_4 = \dot{M}_c c_{p,l}\ T_{4''} + \dot{M}_l c_{p,l} T_1, \tag{39}$$

subcooler (s) - momentum balance

$$p_4 - p_5 = \dot{M}_t R_{u,s}, \tag{40}$$

energy balance

$$Q_s = \dot{M}_t c_{p,l}\left(T_{l,5} - T_{l,4}\right) = \frac{T_{f,a} - T_{l,4}}{R_{t,s}}, \tag{41}$$

pump (p) - momentum balance

$$p_1 - p_6 = \Delta p_p = f\left(\dot{M}_t\right), \tag{42}$$

Overall balances

$$Q_{lg} - Q_c = 0, \tag{43}$$

$$Q_{ph} - Q_s = 0. \tag{44}$$

Eqs. (43) and (44) are solved simultaneously to determine the steady-state operation.

3.1. Loop and model parameters

The conditions (geometric parameters, thermodynamic properties, fixed temperatures, etc.) are listed in Table 1. The relevant hydraulic and thermal resistances and the geometric specifications of the accumulator, condenser, and evaporator are also listed.

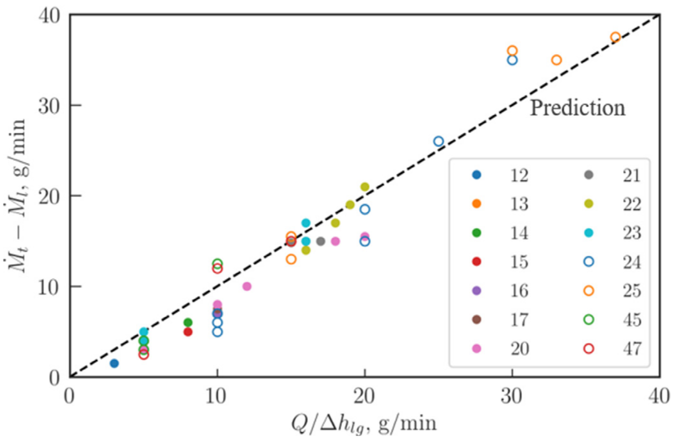

Fig. 8. Comparison of the measured and predicted (broken line) vapor mass flow rate for Tests 12–17, 20–25 and 45–47. The experimental points represent mismatch between measured and predicted mass flow rate in the vapor line, indicating the possibility of an unstable event or measurement error.

3.2. Range of heat and mass flow rates in the tests

Fig. 8 compares of the measured variations in the vapor mass flow rate measured in the experiments as a function of scaled heat load (divided by the heat of evaporation). The vapor mass flow rate is the difference between the total and bypass line mass flow rates, Eq. (37), and the predicted ideal behavior is shown with the straight, broken line from in Eq. (27). The test with measured vapor line mass flow rate above the line, indicates flooding behavior.

Figs. 9(a) and (b) show the predicted flooding and dryout boundaries (dotted lines) by Eqs. (25) and (26), respectively, and the experiments with evaporator 1 using circles, with red circles for dryout, blue for flooding, and black for stable states. Squares show experiments with evaporator 2.

For best fit to experimental results, the predicted boundaries use a wick permeability of 0.2 μm^2, lower than the previously reported value of 0.3 μm^2. This is within the experimental uncertainty reported in Appendix A. Two other limits, namely the predicted liquid channel boil-off limit $Q_{CHF,b} = 1000$ W and the wick superheat limit $Q_{CHF,sh} = 2800$ W, are described in Appendix B, and are outside the limits found experimentally. The regime diagrams obtained from the dynamic stability regimes will be discussed in Section 5.

4. Transient analysis of flooding and dryout

The transient analysis assumes the initially stable state undergoes a sudden change in either the heat load or the mass flow rate and moves toward a new steady state condition. The governing equations are from the steady-state model described in Section 3 but rewritten in transient form and represent the operating condition and the loop architecture. These have been discussed in [28].

As in Section 1, the accumulator controls the liquid temperature at the evaporator inlet and consequently the saturation temperature, so

$$\frac{dT_{e,lg}}{dt} = f\left(p_{lg}(t)\right) = 0. \tag{45}$$

For hybrid loop, a seven-equation model is adopted with the variables being the heater surface temperature T_s; the two-phase fraction of the condenser $V_{c,lg}$; the subcooler temperature $T_{s,l}$; the phase-change mass flow rate $\dot{M}_c$; the bypass line mass flow rate $\dot{M}_l$; and the mass of liquid and vapor in the accumulator $M_{l,a}$ and $M_{g,a}$.

Energy balance – evaporator wall

$$\frac{dT_s}{dt} = \frac{1}{(Mc_p)_{e,w}}\left[Q_{lg} - \frac{T_s - T_{e,lg}}{R_{t,e}} + \frac{T_s - T_l}{R_{t,ph}}\right], \tag{46}$$

LVI condenser – mass balance in the two-phase section of condenser

$$\frac{dV_{c,lg}}{dt} = \frac{1}{\rho_l}\left[\dot{M}_c - \frac{V_{c,lg}}{V_c}\frac{1}{\Delta h_{lg}R_{t,c}}\right.$$
$$\left.\left\{\left[\frac{1}{T_{e,lg}} - \frac{R_g}{M_m \Delta h_{lg}}\ln\left(\frac{p_{e,lg-\dot{M}_{lg}R_{u,g}}}{p_{e,lg}}\right)\right]^{-1} - T_{f,c}\right\}\right], \tag{47}$$

Energy balance - subcooler

$$\frac{dT_{s,l}}{dt} = \frac{1}{(Mc_p)_s}\left[-\dot{M}_t c_{p,l}\left(T_{s,l} - \frac{\left(\dot{M}_c c_{p,c}T_{4''} + \dot{M}_l c_{p,l}T_l\right)}{\dot{M}_t c_{p,l,}}\right)\right.$$
$$\left. - \frac{T_{f,s}}{R_{t,s}} + \frac{1}{R_{t,s}}\frac{\left(\dot{M}_c c_{p,c}T_{4''} + \dot{M}_l c_{p,l}T_l\right)}{\dot{M}_t c_{p,l,}}\right], \tag{48}$$

Mass flow rate, $\dot{M}_{lg} = \frac{(T_s - T_{e,lg})}{R_{t,e}\Delta h_{lg}}$

$$\frac{d\dot{M}_{lg}}{dt} = \frac{1}{R_{t,e}\Delta h_{lg}}\frac{dT_s}{dt}. \tag{49}$$

In the hybrid loop, the hydraulic resistance in the liquid bypass line can be non-zero, so along with Eqs. (46)-(49), an additional mass flow rate is used.

Mass flow rate in the liquid bypass line

$$\frac{d\dot{M}_l}{dt} = -\frac{d\dot{M}_c}{dt}. \tag{50}$$

Mass conservation in the accumulator gas and liquid phases

$$\frac{dM_{g,a}}{dt} = \frac{\rho_g}{\rho_l}\left\{\frac{T_s - T_{e,lg}}{\Delta h_{lg}R_{t,e}} - \frac{1}{\Delta h_{lg}R_{t,c}}\right.$$
$$\left.\times\left[\frac{1}{T_{e,lg}} - \frac{R_g}{M_m \Delta h_{lg}}\ln\left(\frac{p_{e,lg-\dot{M}_{lg}R_{u,g}}}{p_{e,lg}}\right)\right]^{-1} + \frac{T_{f,c}}{\Delta h_{lg}R_{t,c}}\right\}, \tag{51}$$

$$\frac{dM_{l,a}}{dt} = -\left(1 + \frac{\rho_g}{\rho_l}\right)\left\{\frac{T_s - T_{e,lg}}{\Delta h_{lg}R_{t,e}} - \frac{1}{\Delta h_{lg}R_{t,c}}\right.$$
$$\left.\times\left[\frac{1}{T_{e,lg}} - \frac{R_g}{M_m \Delta h_{lg}}\ln\left(\frac{p_{e,lg-\dot{M}_{lg}R_{u,g}}}{p_{e,lg}}\right)\right]^{-1} + \frac{T_{f,c}}{\Delta h_{lg}R_{t,c}}\right\}, \tag{52}$$

The numeric solution to these equations and relevant procedures are discussed in Appendix D.

4.1. Flow rate-based flooding transient behavior

As described in Section 2, the wick is flooded at low heat loads, however, flooding can also occur when the system experiences a significant mass flow rate perturbation from the pump and consequently instantaneous excess liquid flow across the evaporator wick. This flooding modifies the wick thermal resistance with formation of a flood layer with thickness (from mass balance)

$$\delta_l(t) = \int_0^{\tau_f/2} \frac{\dot{M}_t - \dot{M}_l - \dot{M}_c}{\rho_l A_h}dt, \tag{53}$$

and this liquid layer thermal resistance $R_{t,f}$, illustrated in Fig. 10, is

$$R_{t,f}(t) = \frac{\delta_l(t)}{A_h k_l}. \tag{54}$$

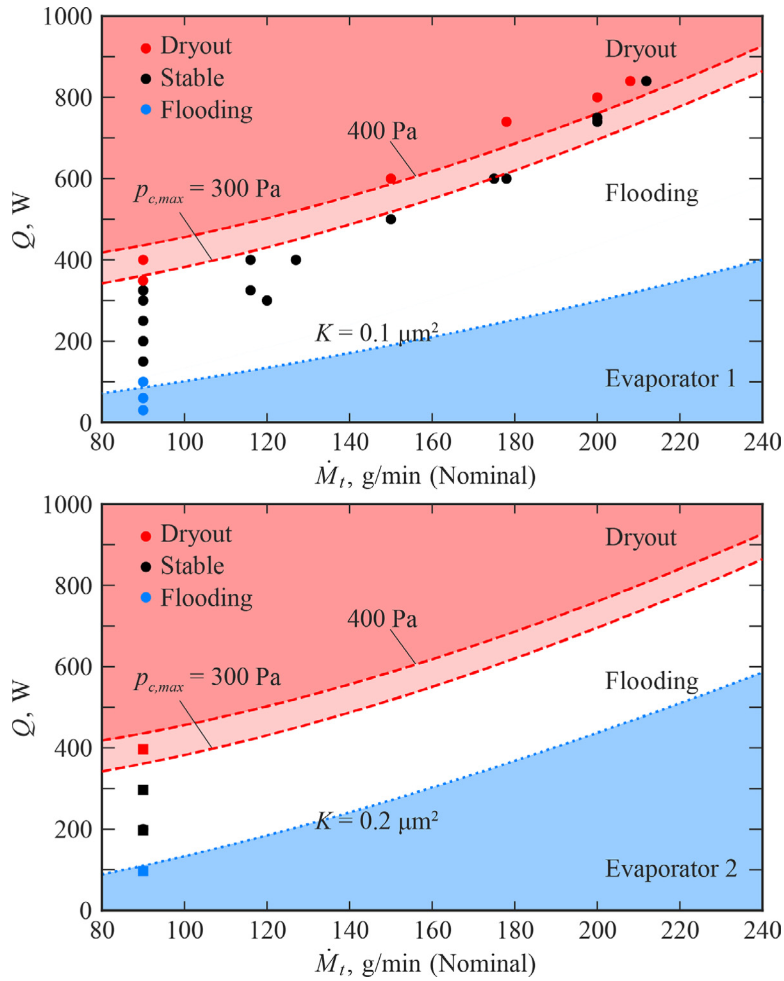

Fig. 9. The operational regime diagram, showing the measured variations of the heat load with respect to the total liquid flow rate for evaporators 1 and 2 as data points. The predicted flooding and dryout boundaries are marked and they are based on the listed values of the evaporator permeability and the maximum capillary pressure. The stable and unstable operating experimental data is show with different colors to match the predicted regimes.

The total thermal evaporator resistance becomes

$$R_{t,e}(t) = R_{t,w} + R_{t,f}(t). \tag{55}$$

Initially, the larger resistance reduces the evaporation rate, causing the heater surface temperature to rise. With this rise the incoming subcooled liquid is more effectively heated and a state is reached where the incoming liquid reaches saturation and liquid preheating is reduced. Then heat flows through the flooded layer, restating the evaporation rate and reducing the liquid layer thickness and decreasing the thermal resistance. This predicted time-dependent pattern is repeated until a new equilibrium point is reached.

Snapshot of this process is illustrated in Fig. 10. Time variations of the flood liquid layer thickness and the two-phase condenser volume fraction are strongly coupled. This is animated in a video in the Supplementary Materials.

Fig. 11 shows the time variations of evaporation rate (under constant hear load), and evaporator inlet temperature for Test 23. The experiments are shown with points and the predictions with lines. The model prediction, Eqs. (45)-(52), are for the time period from 5.5 < t < 7 h, when the heat load is constant at 325 W and the mass flow rate is increased from 90 g/min to 125 g/min. The additional liquid influx shortly floods the wick, causing formation of a liquid layer on top of the evaporator wick, changing its thermal resistance according to Eq. (55). Its immediate effect on the loop is to reduce the evaporation rate, increasing the surface temperature T_s. From Eq. (29), the heat flow redistributes between the evaporation and liquid preheating at the evaporator inlet. The evaporator inlet temperature (subcooled) increases until the surface temperature rise causes the liquid layer to evaporate, reducing the evaporation thermal resistance and increasing the vapor mass flow rate. This pattern is repeated until a new equilibrium point is reached.

By adjusting the evaporator thermal inertia (evaporator mass), the model is capable of predicting both the mass flow rate and temperature oscillations reasonably well. Note that this mode of flooding is based on a steady-state condition followed by a sudden perturbation (discrete change in the pump rotation or a step increase in the heater). In the present considered case, it is a function of the rate at which the pump speed (system level mass flow rate) is increased. If the flowrate is increased at a slow enough rate, oscillations can be avoided.

4.2. Heat load-based dryout transient behavior

The dryout limit is a heat-load based limit predicted by Eq. (25). It is a direct result of insufficient capillary action and mechanical pumping to provide enough liquid for a given heat load, causing a rise in the evaporator temperature. Fig. 7(b) illustrates this for Test 47 (5.6 hr). Dryout can be mitigated by either in-

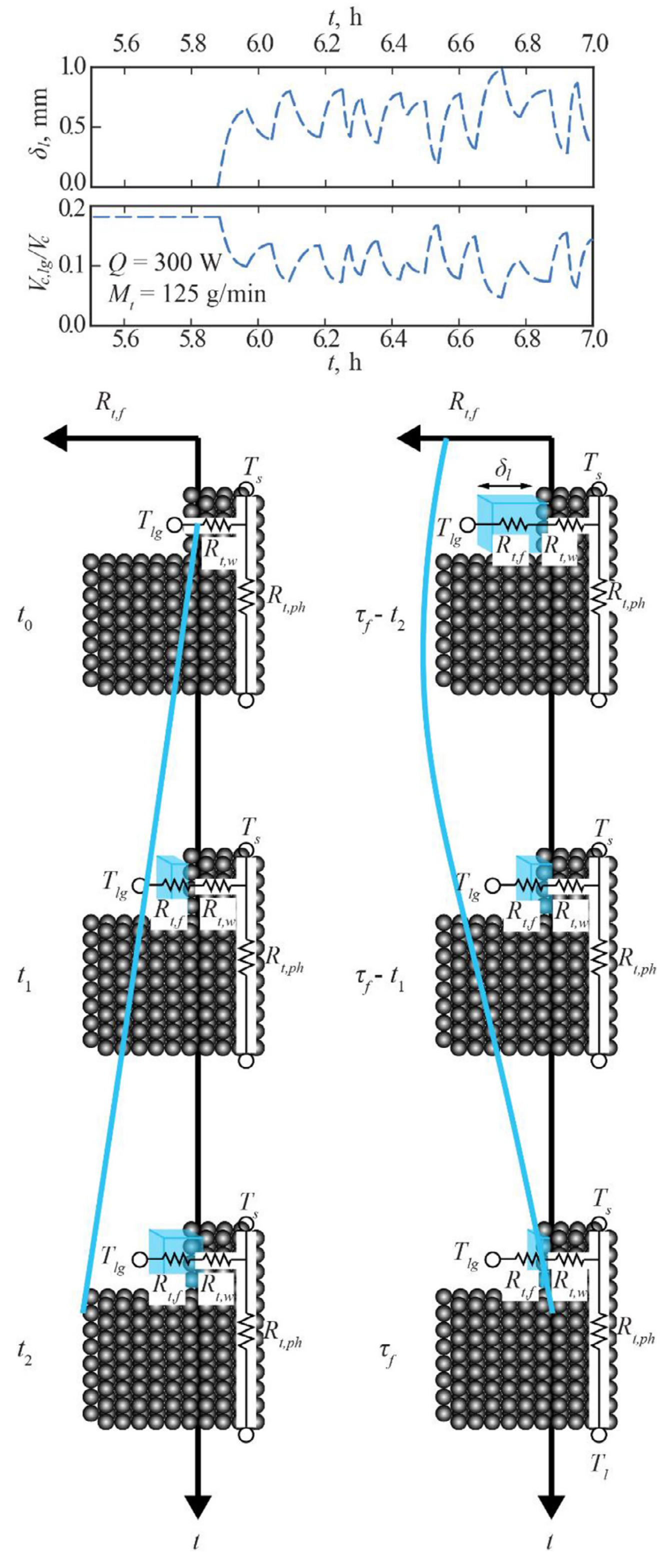

Fig. 10. (a) Animation and graphical time variations of the flooded evaporator liquid layer thickness and the condenser two-phase region (volume fraction). (b) Illustrated snapshots showing the oscillatory pattern of the flooded evaporator thermal resistance. The video is in the Supplementary Materials.

creasing the overall mass flow rate, forcing extra liquid through the wick, or by reducing the heat load. The latter causes the excess heat to disappear instantly, leaving only the thermal response time of the evaporator cooling.

In order to describe the onset of dryout and its mechanism, 3-D CFD simulations of the evaporator 2 are conducted using ANSYS Fluent [29], with the homogenous porous media model as a source term in the Navier-Stokes equation, i.e.,

$$S_i = -\left(\frac{\mu}{K}u_i + C_2\frac{\rho|u|}{2}u_i\right), \tag{56}$$

where K is the wick permeability, and C_2 is the inertial resistance coefficient. The inertial resistance for smooth surfaces is modeled as [23]

$$C_2 = 1.8\frac{1-\varepsilon}{\varepsilon^3 d_p}, \tag{57}$$

where ε is the wick porosity, assumed to be 24% [8,13].

Fig. 12(a) shows a snapshot of the velocity and streamlines distributions inside the wick immediately below the heaters. The heater arrangement is reported in, each heater (102×51 mm^2) is placed at the center of the equally divided evaporator surface, with equal heat loads. Fig. 12(b) shows four snapshots of the pressure distribution in the evaporator wick. This pressure drops due to the wick Δp_w also calculated with the network model, Eq. (23), is listed above each snapshot. The dryout limit is from Eq. (25), taking into account the pressure drops in the vapor line Δp_g and the bypass line and the capillary pressure p_c. The evolution of the dryout front, the dashed black line, under imposed heat load is observed, starting at the center of the heaters at $Q = 330$ W and expanding towards the edges. The largest pressure drop is located in the region immediately below the heaters, indicating the flow is interrupted first at the center of the evaporator. This is in agreement with the infrared surface superheat recording [8]. The partial dryout of the heater surface is modeled with reduced evaporation area and no heat transfer in the dry region, i.e.,

$$R_{t,e,d} = \frac{R_{t,e}}{\left(1 - \frac{A_g}{A_{lg}}\right)}, \tag{58}$$

where A_g is the dryed area, A_{lg} is the vapor groove cross-sectional area, $R_{t,e}$ is given by Eq. (1). The dry region resistance is assumed infinite (no heat transfer) [30].

By repeating the simulation for different heat loads, an expression for the dryout area fraction is

$$\frac{A_g}{A_{lg}} = 0.0016(Q - Q_{CHF,c-v}), \tag{59}$$

where $Q_{CHF,c-v}$ is a function of the mass flow rate, given by Eq. (25). It is equal to 325 W for $\dot{M}_t = 90$ g/min. Eq. (59) is valid for $Q \geq Q_{CHF,c-v}$.

Improvements to Eq. (59) should account for mass flow rate perturbations similar to the flooding event (Section 4.1), which might contribute to dryout prevention.

Fig. 13 compares the predicted and measured time-dependent variations of evaporator outlet temperature for Test 47 [Fig. 7(b)], when the heat load is increased from 300 to 400 W for a brief period, causing the evaporator temperature to increase rapidly. The model is capable of predicting the heating and cooling behavior although with a slightly slower response, which results in a lower peak temperature at the end of 10-minute dryout period. This could be explained by the analysis being first order, i.e., the vapor inertia and/or its dampening effects are not considered. The model prediction is in good agreement with the experiment. Prediction of dryout is extremely important since a large $\Delta Q = Q - Q_{CHF,c-v}$ causes a steep temperature rise and leads to the formation of hotspots and eventually to catastrophic failure.

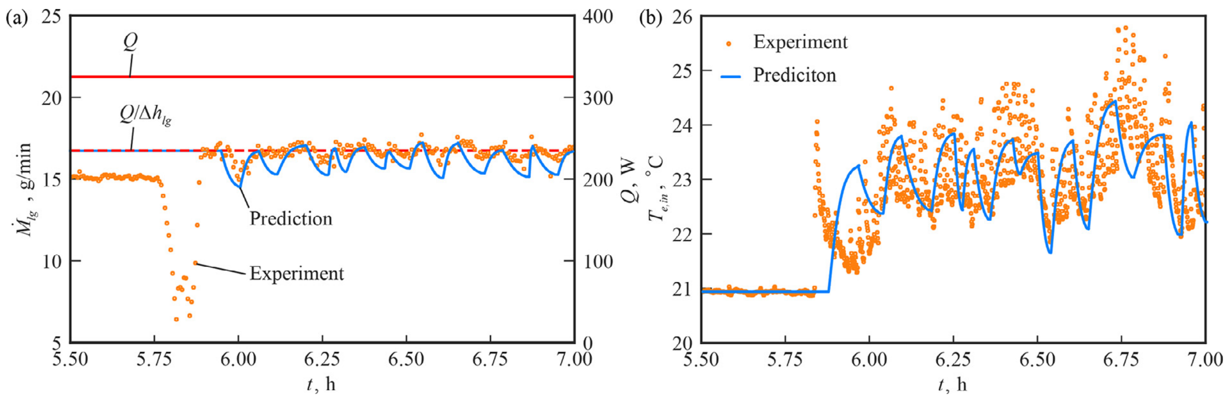

Fig. 11. Time variations of (a) evaporation rate (under constant hear load), and (b) evaporator inlet temperature for Test 23. The experimental results are shown with data points, while the predictions are shown with continuous line.

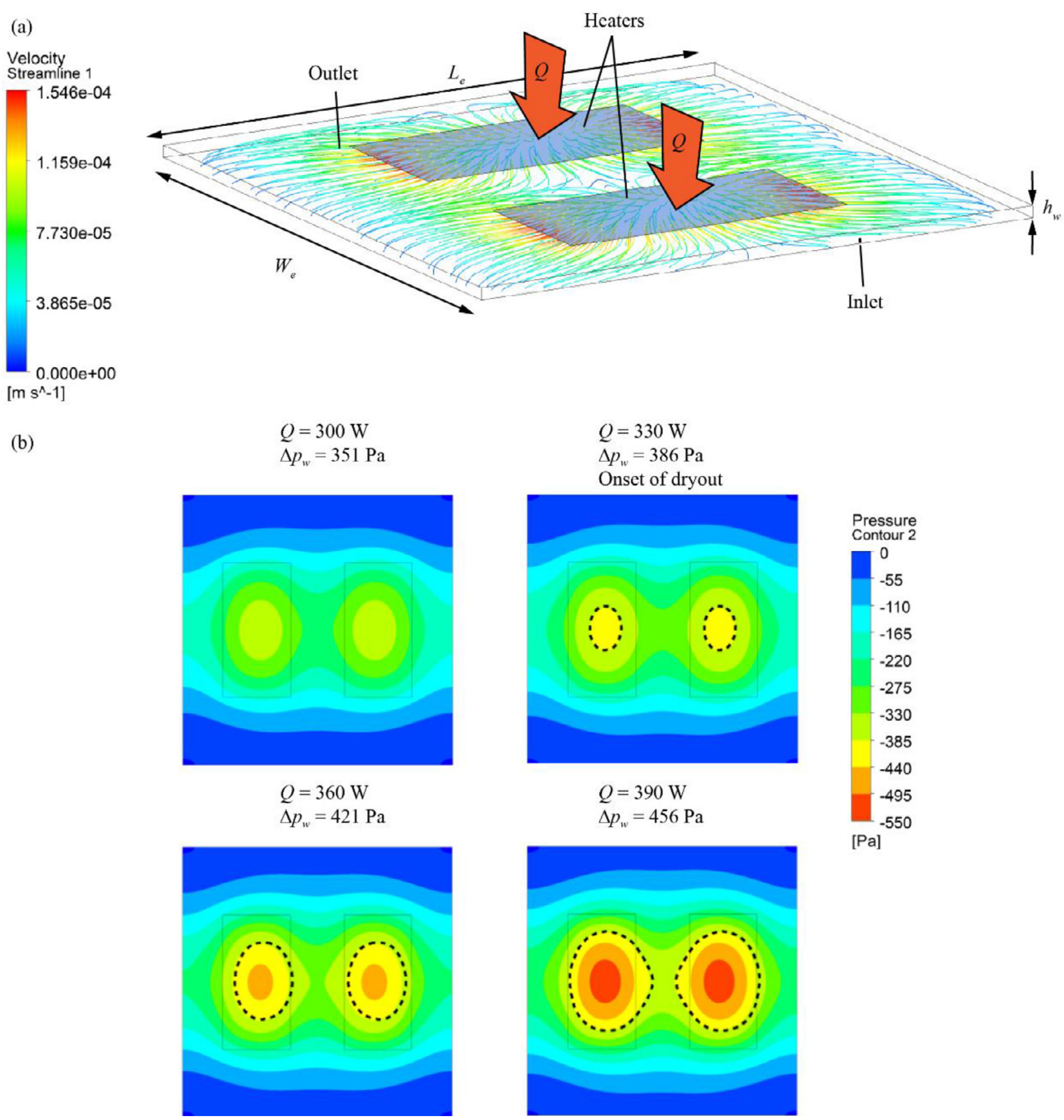

Fig. 12. (a) Snapshot of 3-D evaporator wick simulation showing the liquid velocity distribution and streamlines for $Q = 330$ W. (b) Snapshots of wick liquid pressure drop distribution on the heated surface of the wick, for $\mathbf{Q}$ from 300 to 390 W. The onset of dryout is marked as when the total pressure drop exceeds the maximum capillary pressure.

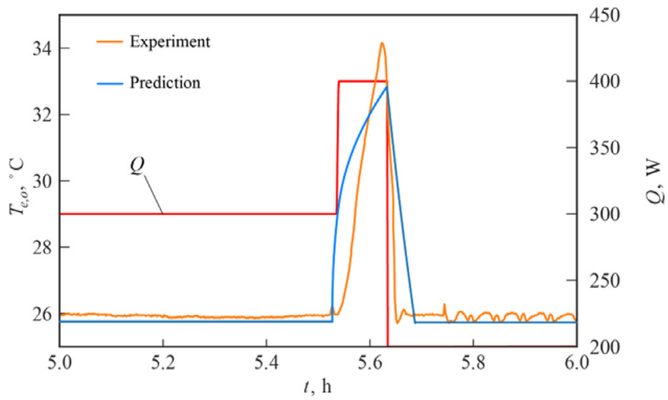

Fig. 13. Time variations of the evaporator exit temperature and controlled, variation heat load, for Test 47. The predicted and measured temperatures are shown.

5. Stability analysis using the system Jacobian

Stability analysis of the system is performed by writing the set of equations from our transient system analysis in vector form $\frac{d\boldsymbol{x}}{dt} = \boldsymbol{f}(\boldsymbol{x})$ where $\boldsymbol{x} = (T_s, V_{c,lg}, T_{sl}, \dot{M}_c, \dot{M}_l, M_{l,a}, M_{g,a})^T$ is the state variable and $\boldsymbol{f}$ is the RHS of Eqs. (46)-(52).

Using a Taylor series expansion about an equilibrium state $\boldsymbol{x_o}$ (the solution to the steady-state system of equations) and disregarding higher order terms, the linearized version of the system is found $\frac{d(\boldsymbol{x}-\boldsymbol{x_o})}{dt} = (\frac{d\boldsymbol{f}}{d\boldsymbol{x}})_{\boldsymbol{x_o}}(\boldsymbol{x}-\boldsymbol{x_o}) = \boldsymbol{J}(\boldsymbol{x}-\boldsymbol{x_o})$ where $\boldsymbol{J}$ is the Jacobian matrix, evaluated at $\boldsymbol{x_o}$.

The solution of $\boldsymbol{x}(t)$ are the linear combinations of $e^{\lambda_k t}$, where λ_k are the eigenvalues of the Jacobian. From the Hartman-Grobman theorem [31], the system will be unstable for $Re(\lambda_i) > 0$. So, by building the Jacobian matrix and finding its eigenvalues, marginal stability diagrams can be constructed based on relevant parameters. The linear stability analysis predicts the ability of the system to reach steady state under state $\boldsymbol{x}$, while the direct time integrations (numerical) described in Section 4 and Appendix D are required to predict the trajectory from state $\boldsymbol{x_o}$ to $\boldsymbol{x}$.

The Jacobian matrix is found by expanding the RHS of Eqs. (46)-(52) and computing the derivatives at the equilibrium point $\boldsymbol{x_o}$. For instance, for Eq. (46)

$$\begin{cases} J_{11} = \frac{\partial}{\partial T_s}\left(\frac{1}{(Mc_p)_{e,w}}\left[Q_{lg} - \frac{T_s - T_{e,lg}}{R_{t,e}} + \frac{T_s - T_l}{R_{t,ps}}\right]\right) = -\frac{1}{(Mc_p)_{e,w}}\left(\frac{1}{R_{t,e}} - \frac{1}{R_{t,ps}}\right) \\ J_{12} = \frac{\partial}{\partial V_{c,lg}}\left(\frac{1}{(Mc_p)_{e,w}}\left[Q_{lg} - \frac{T_s - T_{e,lg}}{R_{t,e}} + \frac{T_s - T_l}{R_{t,ps}}\right]\right) = \frac{1}{(Mc_p)_{e,w}}\frac{(T_{c,lg} - T_{f,c})}{V_c R_{t,c}} \\ J_{13} = \frac{\partial}{\partial T_{sl}}\left(\frac{1}{(Mc_p)_{e,w}}\left[Q_{lg} - \frac{T_s - T_{e,lg}}{R_{t,e}} + \frac{T_s - T_l}{R_{t,ps}}\right]\right) = 0 \\ J_{14} = \frac{\partial}{\partial \dot{M}_c}\left(\frac{1}{(Mc_p)_{e,w}}\left[Q_{lg} - \frac{T_s - T_{e,lg}}{R_{t,e}} + \frac{T_s - T_l}{R_{t,ps}}\right]\right) = \frac{\Delta h_{lg}}{(Mc_p)_{e,w}} \\ J_{15} = \frac{\partial}{\partial \dot{M}_l}\left(\frac{1}{(Mc_p)_{e,w}}\left[Q_{lg} - \frac{T_s - T_{e,lg}}{R_{t,e}} + \frac{T_s - T_l}{R_{t,ps}}\right]\right) = 0 \\ J_{16} = \frac{\partial}{\partial M_{l,a}}\left(\frac{1}{(Mc_p)_{e,w}}\left[Q_{lg} - \frac{T_s - T_{e,lg}}{R_{t,e}} + \frac{T_s - T_l}{R_{t,ps}}\right]\right) = 0 \\ J_{17} = \frac{\partial}{\partial M_{g,a}}\left(\frac{1}{(Mc_p)_{e,w}}\left[Q_{lg} - \frac{T_s - T_{e,lg}}{R_{t,e}} + \frac{T_s - T_l}{R_{t,ps}}\right]\right) = 0 \end{cases}$$

$$J = \begin{pmatrix} J_{11} & J_{12} & 0 & J_{14} & 0 & 0 & 0 \\ J_{21} & J_{22} & 0 & J_{24} & 0 & 0 & 0 \\ J_{31} & J_{32} & J_{33} & J_{34} & J_{35} & 0 & 0 \\ J_{41} & J_{42} & 0 & J_{44} & J_{45} & 0 & 0 \\ J_{51} & J_{52} & 0 & J_{54} & J_{55} & 0 & 0 \\ J_{61} & J_{62} & 0 & J_{64} & 0 & J_{66} & J_{67} \\ J_{71} & J_{72} & 0 & J_{74} & 0 & J_{76} & J_{77} \end{pmatrix}. \tag{60}$$

After repeating this procedure for the remaining variables, the Jacobian matrix can be completed. The eigenvalues are found by solving $\det(\lambda I - J) = 0$. The system's time constant is minus the inverse of the real part of the eigenvalue

$$\tau_i = \frac{-1}{Re(\lambda_i)}. \tag{61}$$

A real eigenvalue indicates a 1st-order type response, exponential growth or decay. The presence of a complex eigenvalue indicates a strong coupling between the two variables, and a 2nd-order type response.

Although the data points inside the stable region in Fig. 9 correspond to $Re(\lambda_i) < 0$, those close to the boundaries have a positive sensitivity coefficient, $\frac{\partial \lambda_i}{\partial x_i} > 0$, where the eigenvalue sensitivity is [32]

$$\frac{\partial \lambda_i}{\partial x} = \eta_i^T \frac{\partial J}{\partial x}\kappa_i, \tag{62}$$

where η_i is the eigenvector of the Jacobian and κ_i the eigenvector of the transposed matrix J. The boundaries in Fig. 9 are produced by identifying the disturbances resulting in sign inversion in the eigenvalues. Furthermore, the analysis of the second-order derivatives of λ_i can also provide interesting results.

Table 3 lists the predicted time constants for Test 23 as the base state. As expected the evaporator thermal time constant $\tau_{t,e}$ is the largest and it is controlled by the thermal mass of the evaporator. Also listed is the evaporator time constant from the measured thermal behavior in Test 23, which is in good agreement with the prediction. The observed other time constants, starting with the subcooler time constant (also listed), are progressively smaller and their experimental observations may require isolation from the evaporator thermal response time constant and this was not attempted here.

In [28], Hoang's analysis separates the problem into three types of physics: fluid dynamics of the line, thermodynamic of the vapor in the reservoir and the vapor space, and thermal at the evaporator. The decay time associated with the former is the fastest, while that associated with the latter is the slowest, reaching hours depending on the thermal capacitance of the heat exchangers. Due to the external control of the thermodynamic state in the accumulator, fixing the saturation pressure in the evaporator, the system behaves in a stiff manner, with barely any influence from the off-diagonal terms in the Jacobian, and no thermodynamic changes are observed in the vapor. In the absence of an external control of the accumulator, Eq. (45) would be included in the transient model and a time constant related to the thermodynamic state of the evaporator is derived. In addition, any fluid dynamics induced fluctuations are filtered (dampened) at lower heat loads due to the relative condenser oversizing. The major source of instabilities is the evaporator, be it due to flooding or dryout, caused by either mass-flow or heat-load perturbations. This type of fluctuations is in agreement with the second type of oscillations described in [33].

In the evaporator time constant, the relationship between the two competing resistances can affect the system marginal stability. Under standard operation, the preheat resistance is larger than the evaporator resistance and the eigenvalue is always negative. When there is an imbalance of mass in the wick, however, the additional flooding resistance appears, and it can change the ratio given below

$$\tau_1 = (Mc_p)_{e,w}\left(\frac{1}{R_{t,e}(t)} - \frac{1}{R_{t,ph}}\right)^{-1}, \tag{63}$$

and causes the system to become unstable when the evaporator resistance overcomes the sensible resistance (due to flooding). This is illustrated in Fig. 14(a) for two different values of Q. From Table 3, the evaporator time constant is 91 s, and this thermal response time generally among the largest.

Similarly, on the condenser side, a relationship for the marginal stability is derived for the condenser time constant, shown in

Table 3
Predicted time constants for the linear response analysis and from experiments, using Test 23 as the base state.

Time constant	Prediction	Experiment	Time constant	Prediction	Experiment
$\tau_1 = \tau_{t,e}$	91 s (0.14 s –182 s)	180 s	$\tau_5 = \tau_{u,l}$	2.3 s	–
$\tau_2 = \tau_{u,c}$	2.3 s	–	$\tau_6 = \tau_{m,a}$	2.7 s	–
$\tau_3 = \tau_{t,s}$	15.2 s	39 s	$\tau_7 = \tau_{m,a}$	1.35 s	–
$\tau_4 = \tau_{u,e}$	2.3 s	–			

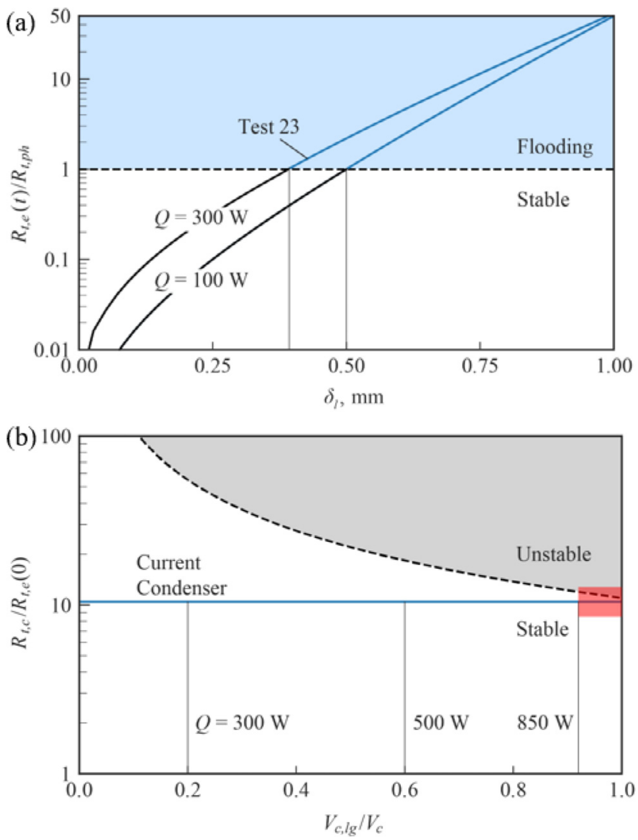

Fig. 14. (a) Dynamic marginal flooding stability showing the maximum evaporator flood liquid thickness as a function of the evaporator thermal resistance scaled with the liquid preheating resistance. The results are for two heat loads, with one corresponding to Test 23. (b) Marginal stability for the condenser to evaporator resistance ratio as function of the condenser two-phase region volume fraction. The blue line shown the current condenser. The volume fraction for three heat loads are also shown. (For interpretation of the references to colour in this figure legend, the reader is referred to the web version of this article.)

Fig. 14(b), normalized by the evaporator baseline resistance.

$$\tau_2 = \rho_l \left[\frac{\Delta p_g - R_{u,g}\dot{M}_{lg}}{\left(1 - \frac{V_{c,lg}}{V_c}\right)^2} - \frac{1}{V_c \Delta h_{lg} R_{t,c}} \right]^{-1}. \quad (64)$$

Fig. 14(b) shows the condenser can lead to instabilities when operating close to its nominal capacity. The current design is stable for low to moderate heat loads, and the condenser time constant of 2.1 s is rather small. This is mostly due to hydrodynamics, and as evident in Table 3, it is faster than thermal response time. At high heat loads near the condenser limit, the system may be under risk of incurring in high frequency oscillations described by Hoang et al. [28] and Launay et al. [33]. The size of the condenser for a given maximum heat load can be found by intersecting the corresponding vertical lines in Fig. 14(b) with the marginal stability line. Based on Fig. 14(b), in order to avoid instabilities in the system, caused or amplified by the condenser, the maximum heat load should be 90 to 95% of the condenser capacity.

Conversely, additional expressions are derived based on the order-of-magnitude analysis. For example, the undersized accumulator and condenser lead to a liquid deficit, as can be deduced from the following relationship for the accumulator time constant

$$\tau_7 = \left[\frac{\frac{1}{\Delta h_{lg}}\left(Q_{lg} - Q_c\right) - \rho_l V_{l,o}}{\rho_l V_{l,o}} \right]^{-1}, \quad (65)$$

the last term on the RHS (also the denominator) represents the initial mass of liquid in the accumulator which is its maximum capacity to replenish liquid loss due to an imbalance between the evaporator and condenser. The time constant for the liquid in the accumulator is very fast, 1.35 s, close to the condenser time constant (since at low heat loads the hydrodynamics dominate, as noted in Table 3. If the required make-up liquid is beyond this limit, the evaporator dryout occurs and this time constant becomes larger.

6. Integration of steady-state, transient, and stability analyses for stable loop design

The steady-state, transient, and stability analyses of Sections 3 to 5 are complementary and provide a thorough description of the thermodynamic, hydrodynamic and thermal behavior of the hybrid CPL. As demonstrated, the analysis enables the prediction of system performance as well as provides the analytic tools to design a system with robust operational characteristics.

The steady-state analysis predicts the isolated/targeted operation conditions of the system and allows for predicting the regime diagram Fig. 9) with the flooding and dryout boundaries defined by Eqs. (25) and ((26). This is in good agreement with experimental data, and allows for determining for example the evaporator wick properties such as the permeability and maximum capillary pressure.

The transient treatment of the system directly tracks time-dependent behavior introduced by sudden perturbations in the heat load or total mass flow rate. The underlying mechanistic processes responsible for flooding and dryout events are included in the model, and are in good agreement with experiments. These are demonstrated in Figs. 10 to 13, tracking time-dependent temperature and pressure at various loop points/states (directly comparable with experiments), as well as liquid, gas, and two-phase dynamics (generally challenging to observe or record experimentally).

The linear response stability analysis builds on the steady-state and transient treatments and provides an analytic insight into the stability of the perturbed states. For a given perturbation, it can predict whether the system will return to an equilibrium state, diverge, or sustain oscillatory behavior. The Jacobian determinant allow for the evaluation of the thermodynamic, hydrodynamic and thermal time constants (relaxation times). Although the Jacobian analysis is limited to the linear response in the transition between states, the scaling treatment allows for developing additional analytic marginal stability conditions, such as Eq. (64). This corresponds to the flooding regime prediction and the stable condenser two-phase behavior shown in Figs. 14(a) and (b). The eigenvalue sensitivity analysis confirms the operation regime boundaries shown in Fig. 9.

The integration of these three analyses provides the theoretical framework for accurate prediction of the system performance (that is in the agreement experimental data and observables), while providing insight into the loop two-phase dynamics which are difficult to observe or record. As a design tool, these treatments allow for component design and sizing, and tuning of the stable operational regimes.

7. Conclusions

In mechanically pumped hybrid CPLs, the forced liquid flow and presence of the liquid bypass line expand the operational limits of the system performance. However, they also lead to a new set of operational instabilities that must be accounted for in the design. The 3D-printed evaporator used in the system presented here allows for novel evaporator geometries as well as the fabrication of a monolithic structure that integrates the wick, the liquid supply and vapor venting passages and the casing. However, the printing process can lead to wick heterogeneity and low porosity (causing low permeability and maximum capillary pressure) which was observed here. At the system level, this reduced wick performance can be compensated for by active pumping.

Among the dominant loop instabilities are the evaporator flooding and dryout. Using the JPL hybrid CPL (with an aluminum alloy evaporator with ammonia as the working fluid) with two different evaporator designs, steady-state and transient analyses are employed, based on the loop mass, momentum, and energy conservation principles, to predict the operational regimes. These are shown to correlate well with the experimental results. The evaporator wick has a thick porous liquid distributor/phase separator with posts emanating from it and directing the liquid to the heated surface, with the vapor escaping between the posts.

The steady-state operational regime diagram (Fig. 8–heat load versus total liquid flow rate) shows both the low capillary-pumping dryout limit of the evaporator wick and the ability to use the pump to achieve much higher dryout limits (up to 850 W). Except for very low heat loads, flooding can be avoided by adjusting the pump flow rate or the hydraulic resistance of the bypass line.

Flooding of the evaporator occurs under excessive liquid supply/insufficient heat supply causing growth of a liquid film in the vapor space which increases the evaporator resistance and the saturation temperature which in turn affects the condenser resulting in a time-varying heater temperature. The 1-D model of the flooding liquid film dynamic predicts this time dependence, and is in good agreement with experimental data.

Dryout occurs in the evaporator when the pressure drop for liquid supply in the wick to the furthest location (central and under the heater) exceeds the available pumping potential. A 3-D CFD simulation of the wick liquid flow shows the dry regions which are ineffective and raise the evaporator resistance. The predicted time-dependent evaporator exit temperature (following the rise and fall in heat load) is in good agreement with experiments.

Finally, using the linear-response and Jacobian dynamical analysis, the stable operational regimes and the associated response time constants of the system (a total of seven) are predicted and are shown to be in general agreement with experimental data. In addition, the analytical coupling between the evaporator and condenser reveals the criterion for the ratio of their resistances for stable operation under variable heat load.

Verified by experiments, it is shown show that the integrated steady-state, transient, and stability analyses described here allow for the design of stable loop that utilize a novel 3D-printed evaporator. The analysis also provides indication of how to improve the performance of the hybrid CPL.

Declaration of Competing Interest

The authors declare that they have no known competing financial interests or personal relationships that could have appeared to influence the work reported in this paper.

Acknowledgments

This research was partly carried out at the Jet Propulsion Laboratory, California Institute of Technology, under a contract with the National Aeronautics and Space Administration. The authors are grateful for the assistance of many personnel at JPL who made this work possible, including Stefano Cappucci, Gaj Birur and Scott Roberts. M.K. and J.F. are thankful for support from NASA-JPL through awards AWD013677 and AWD016859.

Supplementary materials

Supplementary material associated with this article can be found, in the online version, at doi:10.1016/j.ijheatmasstransfer.2021.122019.

Appendix A. 3D-Printed wick properties

A.1. Effective thermal conductivity

Accurate estimation of the 3D-printed evaporator wick properties, e.g., effective thermal conductivity, permeability and capillary pressure, is critical to reliable analysis and model predictions. The effective thermal conductivity and porosity were estimated from the SEM shown in Fig. A.1. With a total of 23 nodes and 37 arms, expressions for one-dimensional heat conduction were written for each arm and the 23 nodal energy equations were solved simultaneously. The effective thermal conductivity was found as $\langle k \rangle =$ 53 W/m-K with a porosity of 25%.

In 3-D printing, the effective thermal conductivity can be larger than predicted by the above correlation, due to severe melting of the powder particles [34].

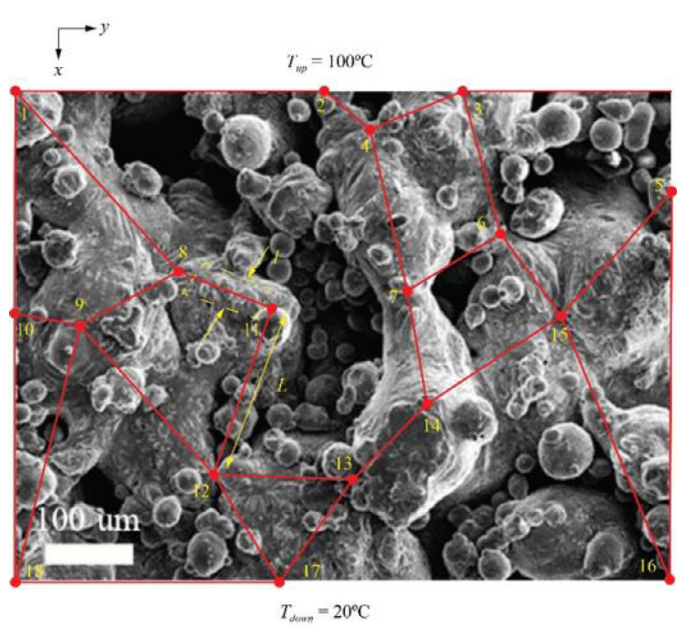

Fig. A.1. 2-D thermal resistance network overlaying the 3-D printed wick SEM micrograph for estimate of the effective thermal conductivity.

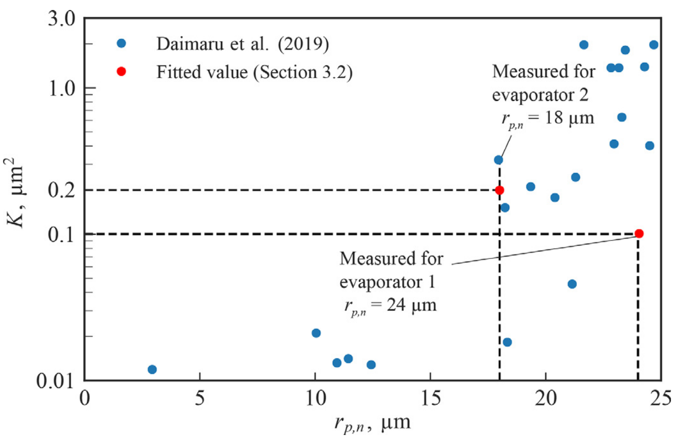

Fig. A.2. Variations of the measured the 3D-printed wick with respect to the nominal pore radius for evaporator 2. The wick used in the JPL tests is marked and has a permeability between 0.2 and 0.3 µm^2.

A.2. Permeability

Measurements of permeability and the respective nominal pore radius for the $AlSi_{10}Mg$ alloy utilized in the 3D printing [23] are shown in Fig. A.2. The pore size of wick samples was taken from bubble point measurements of wick samples and the permeability was derived using Darcy's equation, Eq. (23). The vertical dashed line shows the nominal pore radius in the wick utilized in evaporators 1 and 2 with permeability measurements ranging from 0.15 to 0.3 µm^2. Daimaru et al. [13] adopted $K = 0.3$ µm^2 in their modeling.

The red circle denotes $K = 0.2$ µm^2, the permeability value utilized to fit the experimental data in Section 3.2. It is still within the range of experimental measurements for the nominal pore radius $r_{p,n} = 18$ µm.

Further discussions of the permeability of the 3-D printed wick are available in [35].

Appendix B. Liquid channel boil-off and wick superheat limits

B.1. Liquid channel boil-off limit

The boil-off of the liquid channel is a limiting condition, it occurs when the subcooled liquid in the line surpasses the saturation temperature. The conduction and convection inside the wick are governed by the Péclet number [16]

$$\mathrm{Pe}_L = \frac{\langle u_l \rangle L}{\langle \alpha \rangle}. \tag{B.1}$$

where $\langle u_l \rangle$ is the volume-averaged liquid velocity, L the characteristic length and $\langle \alpha \rangle$ the effective thermal diffusivity. A Péclet number greater than 10 indicates that convection dominates over conduction, if it is smaller than 0.1, conduction is the dominant mechanism of heat transfer. The thermal diffusivity is

$$\langle \alpha \rangle = \frac{\langle k \rangle}{\langle \rho c_p \rangle}. \tag{B.2}$$

with $\langle k \rangle$ and $\langle \rho c_p \rangle$ the effective thermal conductivity and volume-specific thermal capacitance for a porous body. The effective thermal conductivity was discussed in Appendix A and the volume-averaged thermal capacity is $\langle \rho c_p \rangle = \epsilon \langle \rho c_p \rangle_l + (1-\epsilon)\langle \rho c_p \rangle_s$ where subscripts s and l denote solid and liquid phases, respectively, and ϵ is the solid porosity [23]. The volume-averaged wick velocity is related to the liquid mass flux

$$\langle u_l \rangle = \frac{\dot{m}_l A_{lg}}{\rho_l A_w} = \frac{q A_h}{\Delta h_{lg} A_{lg}} \frac{A_{lg}}{\rho_l A_w} = \frac{q A_h}{\rho_l \Delta h_{lg} A_w}. \tag{B.3}$$

For the thermal load of $Q = 850$ W, the Péclet number ranges from 11 at the channel inlet, to 6 at the exit, which means the liquid stream can be heated by conduction when the mass flow rate is very low or the heat load is very high. Fig. B.1(a) illustrates evaporation on the post surface. The snapshot of the CFD simulation shows the temperature distribution for this heat load.

A finite-volume surface convection model is used with temperature boundary condition and

$$\frac{\langle \mathrm{Nu} \rangle_{D,h} k_l}{D_h} A\left(T_{s-l} - \bar{T}_l\right) = \dot{M}_l c_{p,l}\left(T_{l,o} - T_{l,i}\right), \tag{B.4}$$

where $\bar{T}_l = (T_{l,o} - T_{l,i})/2$. The solid-liquid temperature T_{s-l} is determined by

$$T_{s-l,i} = \frac{T_s - T_{s-l,i-1}}{R_{t,ph}\, \dot{M}_l c_{p,l}} + T_{s-l,i-1}, \tag{B.5}$$

where $R_{t,ph}$ is the preheat Peclet resistance, defined as $R_{t,ph} = \frac{h_w}{\langle k \rangle} \frac{(e^{\mathrm{Pe}}-1)}{e^{\mathrm{Pe}}\mathrm{Pe}}$. Equation (B.4) can be written for $T_{l,o}$

$$T_{l,o} = \frac{\frac{\langle \mathrm{Nu} \rangle_{D,h} k_l}{D_h} A T_{s-l} + \dot{M}_l c_{p,l} T_{l,i} - \frac{\langle \mathrm{Nu} \rangle_{D,h} k_l}{2D_h} A T_{l,i}}{\dot{M}_l c_{p,l} + \frac{\langle \mathrm{Nu} \rangle_{D,h} k_l}{2D_h} A}. \tag{B.6}$$

Here $\langle \mathrm{Nu} \rangle_{D,h} = 5.6$ for laminar flow ($\mathrm{Re}_l = 270$) in a rectangular duct with high aspect ratio.

The liquid mass flow rate for each volume has to be updated to account for evaporation

$$\dot{M}_l = \frac{q A_h}{\Delta h_{lg}} \left(1 - \frac{n}{N}\right), \tag{B.7}$$

where n is the volume index and N the total number of volumes (number of posts/fins).

Fig. B.1(b) shows that for a 200 mm long channel, the boil-off limit is not reached with an overall superheat of 20 K. Fig. B.1(c) shows the variation of the total heat leak to the stream. The boil-off limit for $T_s - T_l = 20$ K is found by iteratively calculating the liquid temperature profile for different heat loads.

A heat load of $Q_{CHF,b} = 1000$ W causes the channel to reach the saturation temperature at $y/L_c = 0.9$.

B.2. Wick superheat limit

The wick superheat limit is related to the maximum superheat allowed in the wick

$$q_{CHF,sh} = \frac{\langle k \rangle}{\langle \delta \rangle} \Delta T_{sh,max} = \frac{G}{A} \Delta T_{sh,max}, \tag{B.8}$$

where $\langle\ \rangle$ denotes volume averaged properties, G/A is the thermal conductance (heat transfer coefficient) calculated from CFD simulations and found to be equal to $G/A = 201$ kW/m^2-K and $\Delta T_{sh,max}$ is the maximum superheat (defined as the temperature difference between the substrate and the saturation temperature at the liquid-vapor interface, $T_s - T_{lg}$) before bubble nucleation is observed in the wick [36]. There are different physical models and the following four are considered:

(i) Bubble nucleation theory: the maximum superheat is calculated

$$\Delta T_{sh,max} = \frac{T_{lg}}{\rho_g \Delta h_{lg}} \left(\frac{2\sigma}{r_n} - p_{c,max}\right), \tag{B.9}$$

where r_n is the critical nucleation site radius, a key empirical parameter, dependent on the type of surface. Marcus (1972) [37] uses nucleation theory to derive an expression for r_n for smooth surfaces

$$r_n = \left[\frac{2\sigma T_{lg} k_l}{\Delta h_{lg} q} \left(\frac{1}{\rho_g} - \frac{1}{\rho_l}\right)\right]^{1/2}. \tag{B.10}$$

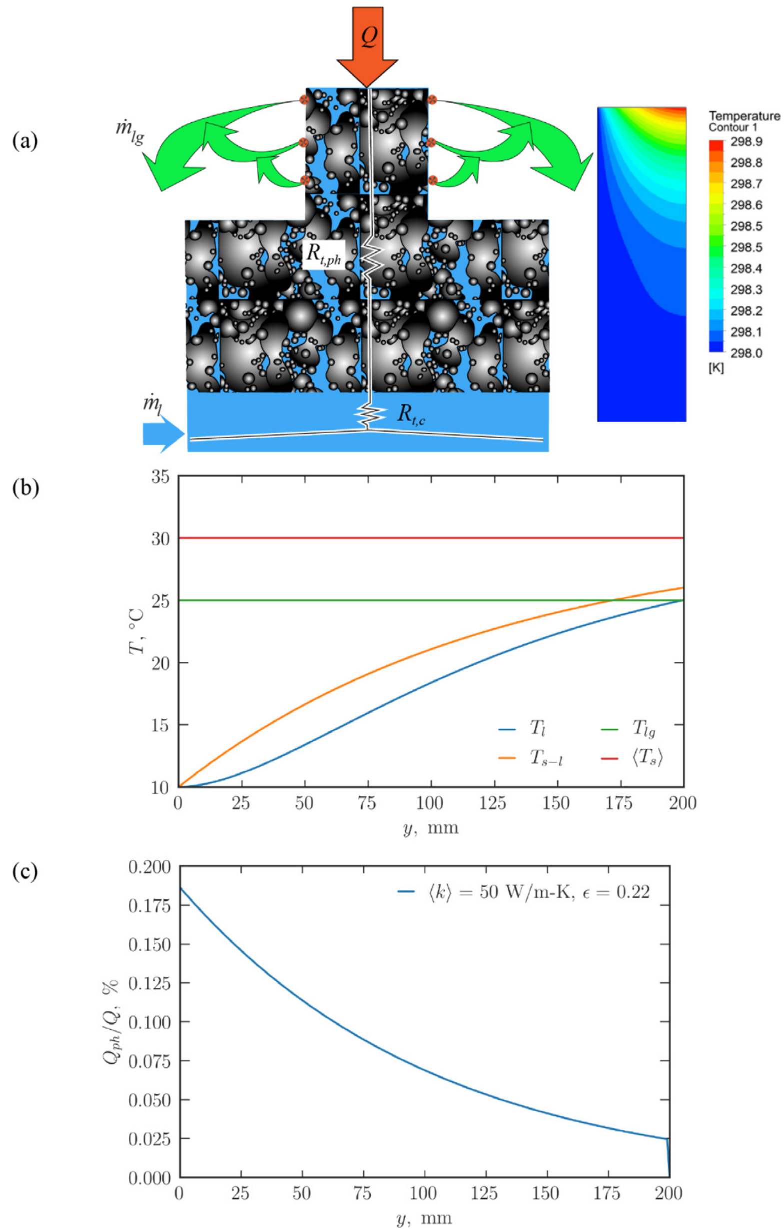

Fig. B.1. (a) The liquid preheat model and the CFD simulated 2D wick temperature distribution. The liquid permeating through wick toward the heater has a negligible effect because the Péclet number is small, it leads to increase of the incoming flow due to upstream conduction. (b) Axial temperature variations of the liquid, wick-liquid, and heater for $\boldsymbol{Q} = 850$ W. The saturation temperature is also shown. (c) The fraction heat load used in liquid preheat.

(ii) Bubble nucleation empirical bubble nucleation radius: Dunn and Reay (1982) [36] suggest r_n between 0.2 and 25 μm and Hwang et al. (2011) [38] observed $r_n = 0.1$ μm for sintered copper particles. The superheat encountered from Eq. (B.9) changes slightly with the wick pore radius.

(iii) Heat flux limit: Daimaru et al. [13] proposed a different superheat limit, based on the maintenance of a liquid bridge between adjacent particles. Based on their experimental observations, this limit can be understood as the absence of bubble nucleation. They calculate the capillary pressure required to maintain this bridge based on geometrical relations.

(iv) Empirical: superheating up to 70 K has been reported in the literature for an ammonia-stainless steel wick [39]. The authors do not disclose if partial dryout was observed.

The superheat limit will depend on wick properties and the physical definition of the bubble nucleation temperature, which can also depend on empirical parameters such as the nucleation radius. Nucleation theory offers a pathway, but it seems to severely underpredict the superheat limit when compared with available empirical evidence.

The bubble nucleation theory (i) is selected since it does not rely on empirical relations. The calculated nucleation radius is $r_n = 0.8$ μm, inside the range proposed in (ii).

The maximum superheat encountered is $\Delta T_{sh,max} = 1.35$ K, which corresponds to the critical heat flux $q_{CHF,sh} = 27.13$ W/cm^2, from Eq. (B.8), or heat load $Q_{CHF,sh} = 2800$ W.

Table C.1
Conditions for Tests 12–17, 20–25, and 45–47.

Test #	$\dot{M}_t$ (g/min)	Q (W)	Evaporator	Event
12	90	65	1	Flooding, T_{amb}
13	90	100	1	Flooding, T_{amb}
14	90	150	1	T_{amb}
15	90	150	1	T_{amb}
16	90	200	1	T_{amb}
17	90	200	1	T_{amb}
20	90	250	1	Dryout
21	90	300–350	1	Dryout, T_{amb}
22	90–125	100–400	1	Flooding, T_{amb}
23	90–116	100–325	1	Flooding
24	90–180	200–600	1	Flooding, dryout
25	90–210	300–850	1	Flooding, dryout
45	90	100–200	2	Flooding
47	90	100–400	2	Dryout, flooding, T_{amb}

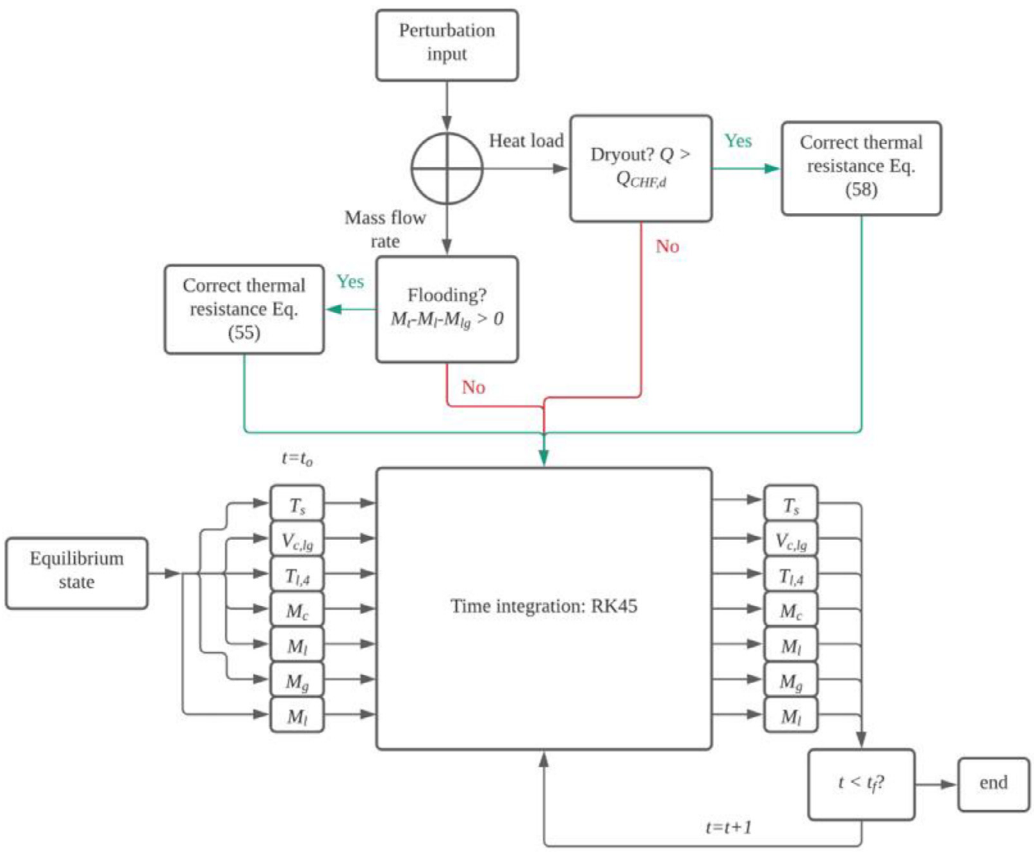

Fig. D.1. Schematic representation of the time-integration algorithm for the system of Eqs. (46)-(52).

Appendix C. Other related tests

The operating conditions of additional tests are listed in Table C.1.

Tests 12–17 and 20–25 are with evaporator 1, while Tests 45 and 47 are with evaporator 2.

Tests 12–17, are constant heat and mass flow rate, ensuring the system capability to reach steady-state operation. Low heat load tests ($Q \leq$ 125 W) led to flooding of the wick discussed in Section 3 and a highly oscillatory behavior was observed.

Tests 20–25, explored the influence of heat load increments, as well as mass flow rate variation. Both dynamic flooding caused by a change in the mass flow rates above the flooding limit discussed in Sections 4 and 5, and dryout caused by heat load increment above the dryout limit, discussed in Section 3, were observed. External intervention is required to remedy both phenomena (reduction of mass flow rate and heat load, respectively.)

The second evaporator is described in detail in [13] and it addresses most of the shortcomings encountered in the operation with evaporator 1 (i.e., the presence of instabilities unrelated to limiting events). Again, dryout and flooding were observed, and the models described in Sections 3 and 4 were capable of predicting the related instabilities.

Appendix D. Calculation procedures

The time integration algorithm for the transient model represented by the system of Eqs. (46)-(52) discussed in Section 4 is shown in Fig. D.1

The initial condition is an equilibrium state, a solution for the steady-state system described in Eqs. (27)-(44) from Section 3.

The seven variables represent the state vector and are input into the time integration solver utilizing the Runge-Kutta RK45 method. The present work utilizes the SciPy implementation in the Python programming language [40].

Currently, the perturbation input can be either a heat load step or a mass flow rate step. Each input type can lead to particular unstable phenomena described in detail in Sections 3 to 5.

For mass flow rate perturbation, a check for the flooding condition is made, Eq. (54), represented by a momentary imbalance between the pump-imposed mass flow rate and the mass flow rates in the phase-change and bypass lines. In case the flooding condition is satisfied, a correction is applied to the evaporator thermal resistance and the solver proceeds.

For heat load perturbations, a check for the dryout condition is made by comparing the current heat load to the dryout limit given by Eq. (25). Again, in case the dryout condition is satisfied, the evaporator thermal resistance is corrected once again, and the information is passed on to the solver.

References

[1] E. Sunada, B. Furst, P. Bhandari, B. Carroll, G. Birur, T. Hendricks, J. Kempenaar, A two-phase mechanically pumped fluid loop for thermal control of deep space science missions, 46th International Conference on Environmental Systems, 2016.

[2] D.G. Gilmore, „ Spacecraft Thermal Control Handbook, Aerospace Press, 2003 M. Donabedian, Ed..

[3] K. Wrenn, D. Wolf, Test Results for a High Power Thermal Management System, in: AIP Conference Proceedings, 2008.

[4] B. Furst, E. Sunada, S. Cappucci, P. Bhandari, A comparison of system architectures for a mechanically pumped two-phase thermal control system, 47th International Conference on Environmental Systems, 2017.

[5] C. Park, J. Zuo, J. Perez, Advanced Hybrid Loop Technology for High Hea Flux Laser Cooling, 3rd International Energy Conversion Engineering Conference, 2005.

[6] T. Hoang, R. Baldauff, K. Cheung, Hybrid Two-Phase Mechanical/Capillary Pumped Loop for High-Capacity Heat Transport, SAE Technical Paper (2007).

[7] J. Ku, Overview of capillary pumped loop technology, National Heat Transfer Conference, 1993.

[8] B. Furst, S. Cappucci, T. Daimaru, E. Sunada, A Mechanically Pumped Two-Phase Fluid Loop for Thermal Control Based on the Capillary Pumped Loop, 49th International Conference on Environmental Systems, 2019.

[9] M. Lee, C. Park, Mechanical-capillary-driven two-phase loop: Numerical modeling and experimental validation, International Journal of Heat and Mass Transfer 125 (2018) 972–982.

[10] W.J. Krotiuk, Thermal Hydraulics for Space Power, Propulsion, and Thermal Management System Design, AIAA, 1990.

[11] L. Ruspini, C. Marcel, A. Clausse, Two-phase flow instabilities: A review, International Journal of Heat and Mass Transfer 71 (2014) 521–548.

[12] S. Chandrasekhar, The stability of superposed fluids: the Kelvin-Helmholtz instability, Hydrodynamic and Hydromagnetic Stability, Dover Publications, 1961 814-514.

[13] T. Daimaru, B. Furst, S.S.E. Cappucci, G. Burr, Development of an Evaporator Using Porous Wick Structure for a Two-Phase Mechanically Pumped Fluid Loop, 49th International Conference on Environmental Systems, 2019.

[14] R. Bradley, D. Pellicone, W. Anderson, Loop Heat Pipe Wick Fabrication via Additive Manufacturing, 47th International Conference on Environmental Systems, 2017.

[15] B. Furst, S. Cappucci, S. Roberts, An Additively Manufactured Evaporator with Integrated Porous Structures for Two-Phase Thermal Control, 48th International Conference on Environmental Systems, 2018.

[16] M. Kaviany, Essentials of Heat Transfer, 1st ed., Cambridge University Press, Cambridge, 2011.

[17] N. Vorayos, N. Katkhaw, T. Kiatsiriroat, A. Nuntaphan, Heat transfer behavior of flat plate having spherical dimpled surfaces, Case Studies in Thermal Engineering 8 (2016) 370–377.

[18] PolyScience, "PolyScience Chiller Manual," [Online]. Available: https://www.polyscience.com/products/chillers/benchtop. [Accessed 22 December 2020].

[19] Swagelok, "Bellows-Sealed Metering Valves," [Online]. Available: https://www.swagelok.com/downloads/webcatalogs/EN/MS-01-23.pdf. [Accessed 22 December 2020].

[20] P. Kundu, I. Cohen, D. Dowling, Chapter 12 - Turbulence, in: Fluid Mechanics, Academic Press, New York, 2016, pp. 603–697.

[21] C.F. Colebrook, C.M. White, Experiments with fluid friction in roughened pipes, in: Proceedings of the Royal Society A, 1937.

[22] C.F. Colebrook, Turbulent flow in pipes, with particular reference to the transition region betweenthe smooth and rough pipe laws, Journal of the Institution of Civil Engineers 11 (4) (1939) 133–156.

[23] M. Kaviany, Principles of Heat Transfer in Porous Media, Springer, New York, 1995.

[24] M. Dobrnjac, Determination of friction coefficient in transition flow region for regular waterworks and pipelines calculation, Annals of Faculty Engineering Hunedoara – International Journal of Engineering (2012) 137–142.

[25] D. Brkić, P. Praks, Unified Friction Formulation from Laminar to Fully Rough Turbulent Flow, Applied Sciences 8 (11) (2018) 2036.

[26] J. Nikuradse, Laws of Flow in Rough Pipes, National Advisory Committee for Aeronautics, Washington, 1950.

[27] I. Bell, J. Wrosnki, S. Quoilin, V. Lemort, Pure and Pseudo-pure Fluid Thermophysical Property Evaluation and the Open-Source Thermophysical Property Library CoolProp, Industrial & Engineering Chemistry Research 53 (6) (2014) 2498–2508.

[28] T. Hoang, R. Baldauff, T. Hollman, J. Maxwell, Nonlinear dynamics in loop heat pipe operation, 46th AIAA Thermophysics Conference, 2016.

[29] ANSYS, "Fluent Reference Manual," 2009. [Online]. Available: https://www.afs.enea.it/project/neptunius/docs/fluent/html/ug/main_pre.htm. [Accessed 21 October 2020].

[30] M. Kim, M. Kaviany, Multi-artery heat-pipe spreader: monolayer-wick receding meniscus transitions and optimal performance, International Journal of Heat and Mass Transfer 112 (2017) 343–353.

[31] D.S. Graça, N. Zhong, H.S. Dumas, The connection between computability of a nonlinear problem and its linearization: The Hartman–Grobman theorem revisited, Theoretical Computer Science 457 (26) (2012) 101–110.

[32] J. Ma, Z. Dong, P. Zhang, Eigenvalue Sensitivity Analysis for Dynamic Power System, *International Conference on Power System Technology*, Chongqing, 2006.

[33] S. Launay, V. Platel, S. Dutour, J.-L. Joly, Transient Modeling of Loop Heat Pipes for the Oscillating Behavior Study, Journal of Thermophysics and Heat Transfer 21 (3) (2007) 487–495.

[34] G. Jacob, A. Donmez, J. Slotwinski, S. Moylan, Measurement of powder bed density in powder bed fusion additive manufacturing processes, Measurement Science and Technology 27 (2016) 115601.

[35] R. Gotoh, B.I. Furst, S.N. Roberts, S. Cappucci, T. Daimaru, E.T. Sunada, Experimental and analytical investigations of AlSi10Mg, Stainless steel, Inconel 625 and Ti-6Al-4V porous materials printed via Powder Bed Fusion, Progress in Additive Manufacturing, submitted (2021).

[36] P. Dunn, D. Reay, Chapter 2 - Theory of the Heat Pipe, in: Heat Pipes, 3rd ed., 1982, pp. 23–89. Oxford, Pergamon.

[37] B.D. Marcus, Theory and design of variable conductance heat pipes, TRW Systems Group, Redondo Beach, CA, 1972.

[38] G.S. Hwang, E. Fleming, B. Carne, S. Sharratt, Y. Nam, P. Dussinger, Y.S. Ju, M. Kaviany, Multi-artery heat-pipe spreader: Lateral liquid supply, International Journal of Heat and Mass Transfer 54 (11-12) (2011) 2334–2340.

[39] M. North, D. Sarraf, J. Rosenfeld, Y. Maydanik, S. Vershinin, High heat flux loop heat pipes, AIP Conference Proceedings 387 (1997) 561–566.

[40] P. Virtanen, R. Gommers, T.E. Oliphant, SciPy 1.0: fundamental algorithms for scientific computing in Python, Nature Methods 17 (2020) 261–272.